Energy 335 (2025) 137917

Contents lists available at ScienceDirect

Energy

journal homepage: www.elsevier.com/locate/energy

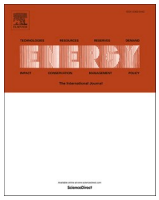

Thermoeconomic and environmental evaluation of a SOFC-driven multigeneration framework integrated with desalination and Electrolysis: Performance assessment and multi-objective optimization

Jing Wang [a], Yonghao Zeng [b], Ming Wang [c,*]

[a] College of Innovation Practice, Liaoning Technical University, Fuxin, Liaoning, 123000, China
[b] School of Mechanical Engineering, Liaoning Technical University, Fuxin, Liaoning, 123000, China
[c] School of Materials Science and Engineering, Liaoning Technical University, Fuxin, Liaoning, 123000, China

ARTICLE INFO

Keywords:
Steam methane reforming
Multi-effect desalination
Solid oxide fuel cell
Thermoeconomic analysis
Net present value
Multi-objective optimization

ABSTRACT

Fuel cells represent a promising avenue for sustainable power generation, offering reduced emissions and high-power density. This study investigates an integrated energy system composed of a solid oxide fuel cell fueled by methane steam reforming, a steam Rankine cycle, a multi-effect desalination unit, and a proton exchange membrane electrolyzer for the simultaneous production of electricity, freshwater, and hydrogen. A comprehensive thermodynamic, economic, and environmental analysis is conducted, supported by sensitivity analysis and multi-objective optimization. The system achieves a total power output of 1039 kW under base conditions, with freshwater and hydrogen production rates of 0.88 kg/s and 0.00175 kg/s, respectively. Thermal and exergetic efficiencies are found to be 33.28 % and 26.87 %. The solid oxide fuel cell contributes the highest exergy destruction (498 kW), while the afterburner exhibits the largest cost rate of exergy destruction at 239,591.65 $/year. The overall payback period is estimated at 5.73 years, and the system reaches an exergoenvironmental impact rate of 14.48 Pt/h. Parametric studies reveal that fuel utilization factor strongly affects power output, and the afterburner's stack flow temperature is a key driver of exergy efficiency. At the optimal design point, net power output improves to 1201.58 kW, freshwater production increases to 0.95 kg/s, and hydrogen generation is 0.0016 kg/s. Additionally, the second-law efficiency improves to 29.86 %, the payback period shortens to 3.63 years, and the exergoenvironmental impact rate is reduced to 13.92 Pt/h. These results confirm the system's viability for integrated energy and resource production with improved performance, economic return, and environmental compatibility.

Nomenclature

Abbreviation		i	Interest Rate [%]
AB	Afterburner	J	Current Density [A/m^2]
AC	Air Compressor	$\dot{m}$	Mass flow rate [kg/s]
CI	Cost Index	N	Operation period in a year [hour]
Cond	Condenser	n	Economic Durability [year]
CRF	Capital Recovery Factor	OC	Operation Cost [$]
FC	Fuel Compressor	P	Pressure [kPa]
MED	Multi-Effect Desalination	$\dot{Q}$	Heat transfer rate [kW]
OFWH	Open Feed Water Heater	R	Ohmic resistance [Ω]
ORC	Organic Rankine Cycle	s	Specific entropy [kJ/kg K]
PEME	Proton Exchange Membrane Electrolyzer	SUCP	Sum Unit Cost of Products [$/GJ]

(*continued on next column*)

(*continued*)

PR	Pressure ratio	T	Temperature [K]
PSO	Particle Swarm Optimizer	U_f	Fuel utilization factor
SCR	Steam to Methane Ratio	$\dot{W}$	Power [kW]
SMR	Steam-Methane Reformer	X	Molar Deduction
SOFC	Solid Oxide Fuel Cell	Z	Cost function [$]
ST	Steam Turbine	$\dot{Z}$	Non-exergetic cost rate [$/year]
Tur	Turbine	**Subscript**	
WP	Water Pump	act	Activation
Symbols		CH	Chemical
AI	Annual Income [$]	conc	Concentration
AS	Annual Saving [$]	fw	Freshwater
B	Brined flow [kg/s]	ohm	Ohmic
BPE	Boiling Point Elevation [°C]	PH	Physical

(*continued on next page*)

* Corresponding author.
E-mail address: wangming@lntu.edu.cn (M. Wang).

https://doi.org/10.1016/j.energy.2025.137917
Received 26 February 2025; Received in revised form 30 July 2025; Accepted 4 August 2025
Available online 6 August 2025

(*continued*)

$\dot{C}$	Cost rate [$/year]	PY	Present year
E	Energy [J]	RY	Reference Year
$\dot{Ex}$	Exergy rate [kW]	**Greek symbol**	
F	Faraday constant/Feedwater	η	Efficiency [%]
FCI	Fixed Capital Investment [$]	φ	Maintenance factor
h	Enthalpy per mass unit [kJ/kg]	μ	Entrainment Ratio

1. Introduction

The challenges of energy and the environment are critical issues facing humanity, exacerbated by the increasing demand for energy [1]. From an environmental standpoint, global warming emerges as the primary challenge posing a significant threat to human life [2]. Global warming results from CO_2 emissions due to fossil fuels utilization [3], while these fuels supply the major share of required energy for power generation, transportation, and heating [4]. This significant energy supply causes almost 80 % of the total CO_2 emissions [5]. While renewable energies are considered environmentally friendly sources, their utilization comes with additional challenges, including intermittency, significant climate change impacts, and lower efficiency [6]. The Solid Oxide Fuel Cell (SOFC) directly converts the chemical energy to power and provides high power generation density and clean stack flow [7]. Besides, its stack flow carries a high temperature, which offers an opportunity to assess different configurations through waste heat recovery [8].

Sadeghi et al. [9] conducted a comparative study on the performance of two solid oxide fuel cell (SOFC) structures: one with an oxygen-ion conducting electrolyte (SOFC-O) and the other with a proton-conducting electrolyte (SOFC-H). Their findings indicated that at current densities below 3000 A/m^2, the SOFC-H exhibited higher efficiency, while the SOFC-O was more suitable for higher current densities. Cammarata et al. [10] explored SOFC performance at the micro-scale, achieving stable power generation with a fuel utilization factor of 70 % and an anode recycling ratio of 60 %. Jiang et al. [11] suggested a biomass-driven SOFC combined with a steam Rankine cycle (SRC) subsystem for power generation, which achieves an exergetic efficiency of 40.09 %. Li et al. [12] combined an internal combustion engine with an SOFC, utilizing the engine's exhaust gas heat with an Organic Rankine Cycle (ORC) for power generation, which resulted in a 58.06 % overall exergetic efficiency. Teng et al. [13] studied a biomass-fueled SOFC integrated with an SRC-TEG cascade, reporting a second-law efficiency of 52.31 % and a value of 3.47 $/GJ as the unit product cost. Hai et al. [14] optimized a methane-fueled SOFC with a supercritical CO_2 cycle for waste heat recovery, achieving an exergetic efficiency of 61.8 %. Cheng et al. [15] proposed a biomass-driven SOFC integrated with an organic flash cycle, reaching an exergetic efficiency of 47.12 % and a 5.50 $/GJ unit product cost. Wang et al. [16] integrated an SOFC, an engine, and a supercritical CO_2 cycle, achieving a 42.28 % second-law efficiency with a 3.34 $/GJ unit product cost and a levelized CO_2 emission of 0.4712 kg/kWh. Liu et al. [17] combined a SOFC and a gas turbine, utilizing the gas turbine's exit flow for boosting a geothermal-driven ORC, which yielded a 14.85 % exergetic efficiency at the optimal SOFC operating temperature.

The waste heat recovery assessment offers the potential to respond to various demands due to the production of different products. Zhu et al. [18] introduced a SOFC-based configuration for co-generating cooling, heating, and power, incorporating a domestic water heater and an Absorption Refrigeration Cycle (ARC). This setup achieved an impressive energy efficiency of 75 % with an operating cost of 410,000 $/year at its optimal state. Ran et al. [19] investigated a micro-scale SOFC cogeneration system that utilized a supercritical carbon dioxide unit and an ARC for waste heat recovery, bringing out a 60.59 % energy efficiency. Tian et al. [20] investigated a biomass-fueled SOFC's wasted heat to raise a geothermal power generation unit, incorporating an ejector refrigeration cycle (ERC) and a domestic water heater subsystem for cooling and heating production and obtained respective first-law of 33.5 % and 61 % second-law efficiency. Liu et al. [21] designed and optimized a SOFC-based multigeneration system from both economic and exergy viewpoints, integrating a transcritical carbon dioxide unit for power and cooling, in conjunction with a domestic water heater subsystem. The results depicted a 62.27 % exergetic efficiency and a 37.12 $/GJ unit product cost. Azhar et al. [22] suggested a SOFC and gas turbine integration with an ORC-LNG heat sink cascade, and a humidification dehumidification for cooling, power, and freshwater production and achieved an exergetic efficiency of 63.29 %. Liu et al. [23] made use of a supercritical CO_2 cycle, a unit for humidification and dehumidification, and an ERC unit to recover SOFC waste heat and obtained a 67.48 % second-law efficiency and 13.94 $/h total cost rate. Soleymani et al. [24] combined a SOFC and a gas turbine unit, directing wasted heat to a biogas-steam reformer for hydrogen production, resulting in 64.65 % exergetic efficiency with a 94 $/GJ unit product price. Tukenmez et al. [25] studied a multigeneration configuration to generate cooling, power, and liquid hydrogen, incorporating a SOFC-gas turbine integration, a supercritical carbon dioxide unit, an ARC-ORC cascade, and a Proton Exchange Membrane Electrolyzer (PEME) and reported energy and exergy efficiencies of about 56.48 % and 54.06 %, respectively. Dai et al. [26] proposed a multigeneration system for power, cooling, heating, and hydrogen production, including a SOFC, a double-stage Rankine and ejector refrigeration unit integration, a thermoelectric generator, and a polymer electrolyte membrane electrolyzer, with an exergetic efficiency of 57.75 % and a unit cost of products of 35.93 $/GJ. Yilmaz and Ozturk [27] assessed a configuration for cooling, power, hydrogen, and ammonia production by merging a SOFC and gas turbine, an ORC, a modified Kalina cycle, an ammonia reactor, and a PEME and reported energy and exergy efficiencies of 61.04 % and 57.13 %, respectively. Adebayo et al. [28] utilized a regenerative ORC, an ARC, a domestic water heater, and a PEME for harnessing wasted heat from a SOFC for power, hydrogen production, cooling, and heating, achieving a 47.4 % energy efficiency. Wang et al. [29] designed a biomass-fueled SOFC with a supercritical CO_2 cycle, a thermoelectric generator, ARC, and a methanation subsystem, recycling a part of the emitted CO_2 and producing hydrogen via the PEME, with a 54.81 % second-law efficiency and a 15.28 $/h total cost rate at the optimum condition. Cao et al. [30] aimed to generate heating, cooling, power, and hydrogen through a SOFC-driven configuration, integrating a supercritical carbon dioxide unit, a gas turbine, a domestic water heater, a LiCl-H_2O ARC, and a PEME and reported an exergetic efficiency of 64.49 % with a unit cost of products as 20.59 $/GJ.

Huang et al. [31] developed a SOFC-powered polygeneration and dehumidification structure integrating a gas turbine, ORC, absorption chiller, and dehumidifier. Their structure produced 551.9 kW of power, 193.0 kW of heating, 20.3 kW of cooling, and dehumidified 1.238 kg/s of air at 14.516 g/kg, with 70.53 % exergy efficiency and 0.301 kg/kWh CO_2 emissions. Multi-objective optimization boosted exergy efficiency to 72.91 %, declined emissions to 0.293 kg/kWh, and increased dehumidified air to 1.606 kg/s. Their suggested structure proved effective in meeting multifunctional energy demands with strong environmental and economic performance. Zheng et al. [32] carried out a comprehensive assessment of a biomass-gasified SOFC-based multigeneration structure integrating transcritical CO_2 cycles, solar desalination, and a PEME to generate power, cooling, freshwater, and hydrogen. Their system delivered 357.6 kW of power, 48.32 kW of cooling, 3.532 kg/h of freshwater, and 2.713 kg/h of hydrogen, with 41.42 % energy and 32.98 % exergy efficiency. Economic evaluation showed a 1.803 $M NPV and a 3.16-year payback period, while environmental analysis identified gasifiers and afterburners as key emission sources. Zhuang et al. [33] assessed a kinetic model-based SOFC structure integrated with RC and KC for elevated waste heat recovery. Employing a microkinetic model for oxygen reduction and dynamic stochastic programming, they optimized the structure for maximum power output. Simultaneous optimization achieved 415.04 kW, a 29.5 % increment

over sequential optimization, and a 10.8 % improvement compared to thermodynamic models.

➢ **Main objectives and novelties**

The literature review emphasizes the potential of SOFC as a sustainable power source and explores its adaptability in various configurations. While complex designs can enhance SOFC-based systems' performance and meet diverse demands, they often incur higher capital investment costs. However, a notable gap in existing literature lies in assessing the overall economic feasibility of these configurations. In response, this study addresses these key objectives by introducing an innovative configuration capable of producing power, freshwater, and hydrogen, while also evaluating its economic viability.

The primary objectives and contributions of the presented assessment are as follows.

- **Proposing a natural gas-fed SOFC:** The utilization of steam reforming of methane reduces CO_2 emissions and fuel costs, enhancing the sustainability of the system.
- **Proposing effective subsystems:** The SOFC's stack flow is efficiently utilized by integrating a steam Rankine cycle with an open water heater, a MED unit, and a PEME.
- **Performing a comprehensive exergy analysis:** Detailed exergy analysis gives insight about the exergy flow inside the system's streamlines and components, visualized through a Sankey diagram, aiding in identifying areas of inefficiency.
- **Performing a comprehensive economic analysis:** Detailed economic analysis evaluates the cost rates of streamlines and components, alongside overall economic viability metrics such as payback period and net present value, providing a holistic perception of the structure's economic feasibility.
- **Performing a comprehensive environmental analysis:** The exergoenvironmental analysis highlights the main sources of environmental footprints due to the performance of the whole structure.
- **Evaluating the configuration's performance through a parametric study:** Parametric analysis assesses the system's performance under varying decision parameter values from multiple points of view.
- **Estimating the optimal operating mode:** The optimization procedure considers both economic and thermodynamic viewpoints through diverse multi-objective optimization scenarios, aiming to identify the optimum operating condition that maximizes performance and economic efficiency.

➢ **Paper's structure**

The paper's contents are summarily indicated in this section to clarify the conducted studies. The designed configuration is described in section 2, including the operating mode of the different parts. Section 3 illustrates the modeling procedure in which the economic, thermodynamic, and optimization assessments are discussed. Section 4 stands out for the analysis outcomes in terms of validation, baseline outputs, parametric assessment, and optimization results. Ultimately, Section 5 summarizes the key reports as conclusions.

An overview of the paper's contents is given in this section to elucidate the studies conducted.

- Section 2: Configuration Description describes the proposed configuration in detail, including the operation of different components such as the SOFC, steam Rankine cycle, MED unit, and PEME.
- Section 3: Simulation Procedure discusses the methodology used for simulation, encompassing thermodynamic, economic, and optimization assessments.
- Section 4: Analysis and Results presents the outcomes of the analysis, including validation of the model, baseline results, sensitivity analysis, and optimization results to identify the optimal operating conditions.
- Section 5: Conclusions summarizes the key findings of the study and discusses the implications of the results, highlighting the significance of the proposed configuration and its economic viability.

2. The Configuration Description

The configuration's overall schematic, depicted in Fig. 1, encompasses the SOFC, steam Rankine cycle, MED, and PEME. Each unit is described below:

The SOFC unit is supplied with methane via steam reforming. Methane (state 3) is initially compressed by the fuel compressor (FC) and preheated in heat exchanger 2 (HX2) before entering the mixer (Mix) as state 6. Simultaneously, feed water (state 1) is pressurized by the water pump (WP) and heated in HX3 to reach the saturated liquid state. The saturated liquid (state 3) is mixed with methane and enters the reformer (SMR). Heat for the reforming process is provided by the stack flow, producing syngas (state 8) to feed the SOFC's anode. Ambient air, compressed by the air compressor (AC) and heated in HX1, feeds the SOFC's cathode, enabling power generation through the interaction of cathode and anode feed flows. Exit flows from these units are divided into two streams: the first stream is recycled to the anode (state 11) and cathode (state 18), while the remaining streams are directed to the afterburner (AB). Within the AB, syngas and air undergo combustion, supplying the necessary heat for the subsystems and reforming process. The combustion's stack flow crosses various components, including REF, HXs 2, 3, 1, the boiler, MED's first stage, and HX5.

In the steam Rankine cycle, the condenser's exit flow (state 31) is pressurized by pump 1 (Pu1) before reaching the open feedwater heater (OFWH). The OFWH's exit flow, saturated water, is pressurized by Pu2 to reach the boiler's operating pressure. This pressurized water then turns into superheated steam to enter the turbine (Tur, state 28). The turbine, implemented as a two-stage system, extracts a portion of the steam in the high-pressure section to supply the OFWH, while the remaining steam is expanded to generate power. Finally, the turbine's exit flow returns to the condenser, completing the cycle's loop.

Within the MED unit, feed seawater is initially preheated in HX6 before being sprayed into the stages. In each stage, the sprayed saline water evaporates and is collected to advance to the subsequent stage. These vapors become saturated through heat transfer processes in the subsequent stages, producing freshwater. Since each stage receives input energy from the preceding stage for the evaporation process, the first stage's input heat is supplied by an external heat source. Ultimately, saturated vapors are collected as freshwater.

In the PEME, feed water is heated in HX5 before reaching the desired electrolyzer temperature through the process denoted as 66 → 67. The feed water then enters the electrolyzer, where electrolysis separates it into O_2 and H_2, which are stored in the respective tanks.

Based on the abovementioned descriptions, the selection of a SOFC as the primary energy conversion unit is based on its high operating temperature and associated thermal benefits. The SOFC produces high-grade exhaust heat that is ideal for thermal integration across several subsystems. After enhancement via post-combustion, this heat is effectively used for.

- Supplying endothermic heat to the steam methane reformer,
- Preheating the fuel and oxidant inlet streams,
- Generating additional power via a steam Rankine cycle, and
- Driving the thermal desalination process through a multi-effect desalination unit.

These synergistic interactions maximize the overall energy utilization and minimize exergy destruction, thereby justifying the use of SOFC in this multigeneration structure.

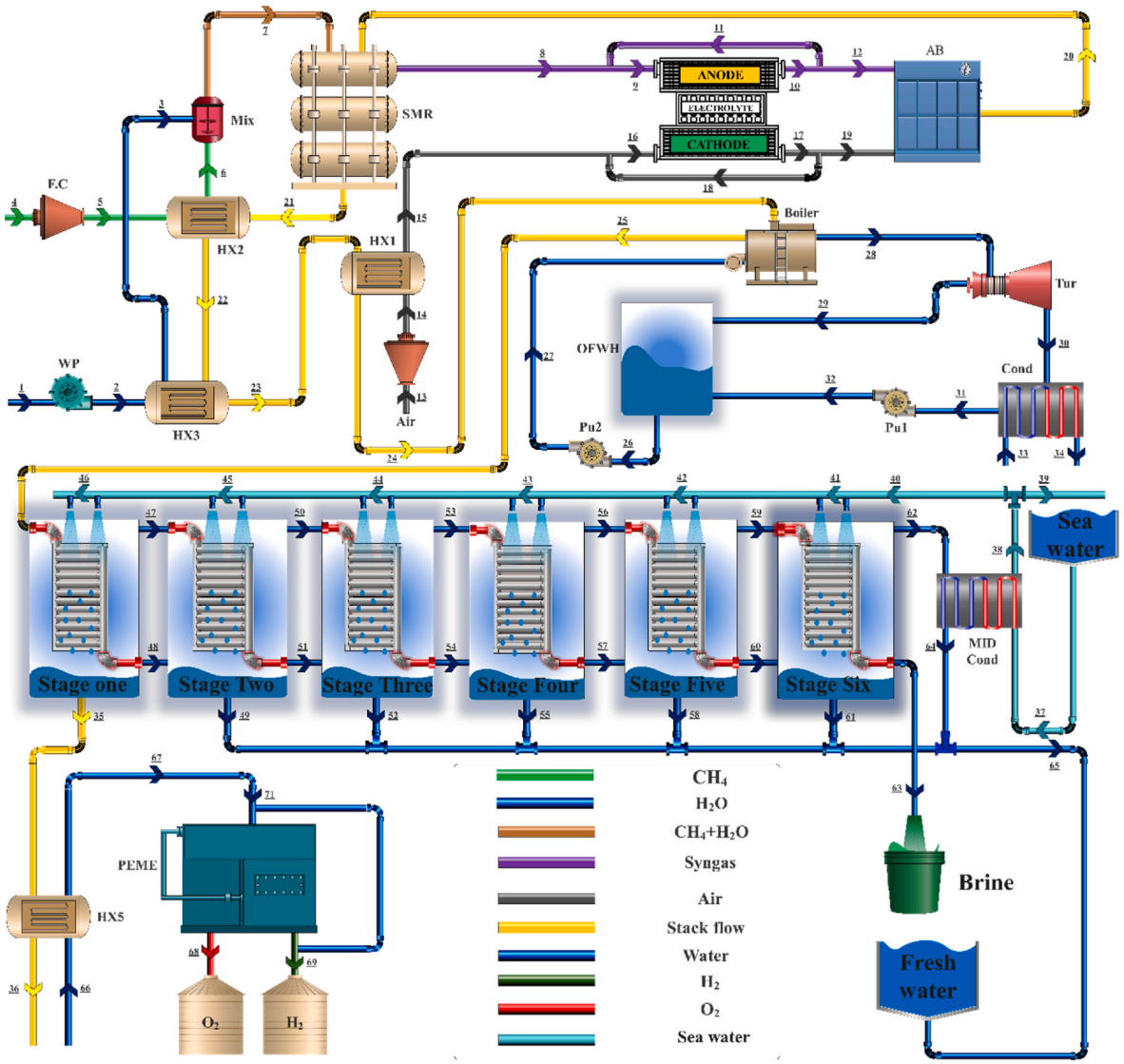

Fig. 1. The schematic of the presented structure.

3. The simulation procedure

The simulation process involves the integration of thermodynamic, economic, and optimization approaches, which introduces a significant level of complexity. Several assumptions are taken into consideration to streamline the modeling process.

1. Steady-state conditions: The modeling process is carried out under steady-state conditions to facilitate the analysis [34].
2. Neglect of potential and kinetic energies: Kinetic and potential energies are neglected through the exergy and energy balances to simplify the calculations [35].
3. Components treated as adiabatic control volumes: The components are handled as control volumes that are adiabatic to simplify the modeling of heat transfer processes [36].
4. Neglect of pressure drops: The simulation procedure does not account for pressure drops in pipelines and heat exchangers to streamline the analysis [37].
5. Specific isentropic efficiency: Pumps, compressors, and turbines are assumed to operate at specific isentropic efficiencies for simplicity [37].

3.1. Thermodynamic viewpoint

The thermodynamic evaluation entails the scrutiny of mass, energy, and exergy equilibrium equations, which are explained in this subsection. The mass balance evaluation encompasses both the chemical reactions through the reforming unit and other components' mass balance. The reforming process is mathematically represented as follows [38]:

$$CH_4 + H_2O \rightarrow CO + 3H_2 \quad (1)$$

$$CO + H_2O \rightarrow CO_2 + H_2 \quad (2)$$

$$n_1CH_4 + n_2H_2O \rightarrow n_3CH_4 + n_4H_2 + n_5H_2O + n_6CO + n_7CO_2 \quad (3)$$

The chemical reactions associated with the SOFC unit are outlined below [39]:

$$0.5O_2 + H_2 \rightarrow H_2O + \dot{W}_{elec} \quad (4)$$

The PEME comprises the reaction below [40]:

$$H_2O + \dot{W}_{elec} \rightarrow 0.5O_2 + H_2 \quad (5)$$

The components' mass balance is indicated as [41]:

$$\sum \dot{m}_{in} = \sum \dot{m}_{out} \quad (6)$$

Herein, ṁ represents the rate of mass flow.

The energetic and exergetic equilibrium equations are defined as follows [41]:

$$\dot{Q}_{C.V} - \dot{W}_{C.V} = \sum (\dot{m}h)_{in} - \sum (\dot{m}h)_{out} \tag{7}$$

$$\dot{E}x_Q - \dot{E}x_W + \dot{E}x_D = \sum \dot{m}_{out} ex_{out} - \sum \dot{m}_{in} ex_{in} \tag{8}$$

Terms $\dot{Q}$, $\dot{W}$, and $\dot{E}x$ depict the respective rates of heat transfer, work, and exergy. Terms h and ex refer to the enthalpy per mass unit and exergy. Since the designed system includes chemical reaction, ex involves the chemical (CH) and physical (PH) parts, which are calculable as follows [42]:

$$ex^{PH} = (h - h_0) - T_0(s - s_0) \tag{9}$$

$$ex^{CH} = \sum X_i ex_i^{CH} + \overline{R}T_0 \sum X_i \ln X_i \tag{10}$$

where T is the temperature, s refers to the entropy per mass unit, and X depicts the molar fraction.

The SOFC and PEME involve electrolysis processes that entail plenty of additional equations. The electrolysis process's needed voltage (V) in the SOFC is described below [43]:

$$V_{SOFC} = V_{Nernst} + V_{act,i} + V_{conc,i} + V_{ohm}; \quad i = A, C \tag{11}$$

where the subscripts conc, act, and ohm symbolize the concentration, activation, and ohmic terms, respectively. Besides, C and A denote the cathode and anode. The Nernst potential (E_{Nernst}) is achievable as follows [43]:

$$E_{Nernst} = E_{rev}(T, P) - \frac{RT}{nF} \ln \frac{P_{H_2} P_{O_2}^{0.5}}{P_{H_2O}} \tag{12}$$

$$E_{rev}(T, P) = -\frac{\Delta G(T, P)}{nF} \tag{13}$$

In these equations, n shows the transferred electrons, P signifies pressure, F refers to the Faraday constant, and ΔG symbolizes the Gibbs free energy. Moreover, the value of the activation potential is computable as follows [43]:

$$E_{act,i} = \frac{RT}{F} \sinh^{-1}\left(\frac{J}{2J_{0,i}}\right) \tag{14}$$

$$J = J_{0,i}\left[\exp\left(\frac{\alpha n F E_{act,i}}{RT}\right) - \exp\left(-\frac{(1-\alpha) n F E_{act,i}}{RT}\right)\right] \tag{15}$$

$$J_{0,i} = \gamma_i \exp\left(\frac{E_{act,i}}{RT}\right) \tag{16}$$

where J denotes the current density, J_0 shows the exchange current density, α represents the charge transfer coefficient, and γ signifies the pre-exponential factor. The calculation of the concentration potential can be carried out by the following process [43]:

$$E_{conc} = -\frac{RT}{2F} \ln\left(1 - \frac{J}{2J_{L,C}}\right) + \frac{RT}{2F} \ln\left(1 + \frac{P_{H_2} J}{P_{H_2O} J_{L,C}}\right) - \frac{RT}{4F} \ln\left(1 + \frac{P_{H_2} J}{P_{H_2O} J_{L,A}}\right) \tag{17}$$

$$J_{L,A} = \frac{4F P_{O_2,A} D_A^{EFF}}{\left(\frac{P - P_{O_2,A}}{P}\right) RT\delta_A} \tag{18}$$

$$J_{L,C} = \frac{2F P_{H_2,E} D_C^{EFF}}{RT\delta_C} \tag{19}$$

where D^{EFF} indicates the effective coefficient of diffusion, δ stands for the elements' thickness, and J_L refers to the limiting current. The ohmic potential can be evaluated as [44]:

$$J_{L,C} = (\zeta_A \delta_A + \zeta_C \delta_C + \zeta_E \delta_E) J \tag{20}$$

where the term ζ outlines the resistivity of the material. Ultimately, the power generation associated with each cell is estimated as follows [44]:

$$\dot{W}_{elec} = EJ \tag{21}$$

The required input activation energy for the PEM electrolyzer for water decomposition is defined as follows [40]:

$$\Delta H = \Delta G + T\Delta S \tag{22}$$

Besides, the overall electrical potential associated with the electrolysis criterion is calculated below [40]:

$$V = V_0 + V_{act,A} + V_{act,C} + V_{ohm} \tag{23}$$

These terms are estimated as [45]:

$$V_0 = 1.229 - 8.5 \times 10^{-4} \times [T_{PEM} - 298] \tag{24}$$

$$\begin{cases} V_{act,A} = \frac{RT}{F} \times \sinh^{-1}\left[\frac{J}{2J_{0,A}}\right] \\ V_{act,C} = \frac{RT}{F} \times \sinh^{-1}\left[\frac{J}{2J_{0,C}}\right] \end{cases} \tag{25}$$

$$V_{ohm} = J \times R_{PEM} \tag{26}$$

Also, J_0 for the cathode and anode is computed as follows [45]:

$$\begin{cases} J_{0,a} = J_a^{ref} \times e^{\left[-\frac{E_{act,a}}{RT}\right]} \\ J_{0,c} = J_c^{ref} \times e^{\left[-\frac{E_{act,c}}{RT}\right]} \end{cases} \tag{27}$$

$$R_{PEM} = \int_0^d \frac{dx}{\sigma_{PEM}[\lambda(x)]} \tag{28}$$

J^{ref} is the pre-exponential variable and R_{PEM} refers to the Ohmic resistance. Furthermore, λ(x) symbolizes the water content, and σ(x) expresses the local ionic conductivity. The mentioned terms are obtained as follows [45]:

$$\sigma_{PEM}[\lambda(x)] = [-0.326 + 0.5139 \times \lambda(x)] \times e^{1268 \times \left[\frac{1}{303} - \frac{1}{T}\right]} \tag{29}$$

$$\lambda(x) = \frac{\lambda_a - \lambda_c}{L} \times x + \lambda_c \tag{30}$$

where L denotes the membrane's thickness. In the final step, the hydrogen and oxygen production molar rates are computed as [46]:

$$\dot{N}_{H_2} = \frac{J}{2F} \tag{31}$$

$$\dot{N}_{O_2} = \frac{J}{4F} \tag{32}$$

The initial step in the MED modeling involves setting up temperatures to assess the temperature at which each step operates. Given that the MED comprises multiple stages, it is assumed that the temperature difference (T) of the brined flow between each consecutive stage remains constant. This constant temperature difference is determined as [47]:

$$\Delta T = (T_1 - T_n) / n \tag{33}$$

In this way, each stage's temperature is attained as [47]:

$$T_{i+1} = T_i + \Delta T \quad i = 1, 2, \ldots, n \tag{34}$$

The second approach involves determining the saline water's evaporation temperature (T_v), which considers the Boiling Point Elevation (BPE) term. Thus, the T_v for each stage is calculated as [47]:

$$T_{v_n} = T_n - BPE_n \tag{35}$$

The third approach concerns the brined water flow (B). As previously noted, the assessment of terms for the beginning is conducted independently of the following phases. In this context, the flow of brined water in the first step is established as [47]:

$$B_1 = F_1 - D_1 \tag{36}$$

The terms D and F represent the desalinated vapor flow and feed water, respectively. The desalinated flow rate is determined using the following formula for the first stage [47]:

$$D_1 = \left(D_0\left(h_d - h_{fd}\right) - F_1 C_p (T_1 - T_F)\right) / \lambda_1 \tag{37}$$

Where λ and C_p denote the evaporation's specific latent heat and specific heat capacity, respectively. The fourth approach focuses on estimating the brine salinity (Y_b), which stage one's term is estimated as follows [47]:

$$Y_{b_1} = (F_1/F_1 - D_1) Y_F \tag{38}$$

In this regard, other stages' terms are obtained as [47]:

$$D_i = \left((D_{i-1})\lambda_{i-1} - F_i C_p (T_i - T_F) + B_{i-1} C_p (T_{i-1} - T_i)\right) / \lambda_i \tag{39}$$

$$B_i = B_{i-1} + F_i - D_i = (B_{i-2} + F_{i-1} - D_{i-1}) + F_i - D_i = \sum_{k=1}^{i} F_k - D_k \tag{40}$$

$$Y_{b_i} = \left(Y_F F_i + Y_{b_{i-1}} B_{i-1}\right) / B_i \tag{41}$$

Finally, the MED freshwater production rate is obtained as [47]:

$$\dot{m}_{fw} = \sum_{i=1}^{n} D_i \tag{42}$$

! Note: Table S1 in the supplementary file indicates the components' energy, mass, and exergy balances.

3.2. The economic viewpoint

Economic simulation is conducted through the exergoeconomic approach, which incorporates the exergy cost per mass unit (c). The components' cost balance is outlined as follows [48]:

$$\sum \dot{C}_{in,k} + \dot{Z}_k = \sum \dot{C}_{out,k} \tag{43}$$

$$\dot{C} = c\dot{E}x \tag{44}$$

In these equations, $\dot{C}$ expresses the rate of cost. $\dot{Z}_k$ signifies the rate of total cost for the component and is computed by use of the following expression [48]:

$$\dot{Z}_k = \frac{CRF \times \varphi}{N \times 3600} \times \frac{CI_{PY}}{CI_{RY}} \times Z_k \tag{45}$$

$$CRF = \frac{i(1+i)^n}{(1+i)^n - 1} \tag{46}$$

In which N, n, CRF, φ, and i stand for the operating hours in a year, economic lifetime, capital recovery factor, maintenance factor, and interest rate, respectively. Z_k signifies the reference year cost function associated with each component. Subsequently, the Cost Index (CI) is employed to upgrade Z_k to the present year. Table 1 demonstrates the components' cost function and associated CI and reference year. Additionally, the components' cost balances are represented in Table S.2 of the supplementary file.

Table 1
The cost functions for each component.

Components	Purchase cost function	CI	Ref. year	Reference
FC	$Z_{FC} = 91562 \times (\dot{W}_{FC}/455)^{0.67}$	368	1994	[1]
WP	$Z_{WP} = 3540(\dot{W}_{FWP})^{0.71}$	550.08	2010	[1]
AB	$Z_{AB} = (46.08 \times \dot{m}_{17}/(0.995 - P_{out}(P_{in}))[1 + \exp(0.018 \times T_{AB} - 26.4]$	368	1994	[49]
AC	$Z_{AC} = 91562 \times (\dot{W}_{AC}/455)^{0.67}$	368	1994	[1]
SMR	$Z_{SMR} = 283 \times \dot{Q}_{SMR}$	668	2020	[38]
SOFC	$Z_{SOFC} = A_{act} \times N_{cell}(2.9 \times T_{cell} - 1907)$	395.6	2002	[49]
HX	$Z_{HX} = 130\left(\frac{A_{Hx}}{0.093}\right)^{0.78}$	468.2	2005	[49]
Cond	$Z_{Cond} = 130\left(\frac{A_{Cond}}{0.093}\right)^{0.78}$	468.2	2005	[1]
ST	$Z_{ST} = 4605 \times (\dot{W}_{ST})^{0.7}$	402.3	2003	[50]
Pump	$Z_{Pu} = 3540(\dot{W}_{Pu})^{0.71}$	550.08	2010	[1]
PEME	$Z_{PEME} = 1000 \times (\dot{W}_{PEME})$	668	2020	[1]
OFWH	$Z_{OFWH} = \left(\frac{527.7}{397}\right)^{1.7} \times (C_{OFWH})\text{Log}(C_{OFWH}) = 4.2 - 0.204 \times \text{Log}(\dot{m}_{out}) + 0.1245 \times (\log(\dot{m}_{out}))^2$	468.2	2005	[50]
MED	$Z_{MED} = 6291 \times \dot{m}_{FW}^{0.865} \times \left[1 - f_{HE} + f_{HE} \times \left(\frac{N_{stage}}{N_{ref}}\right)^{1.277} \times \left(\frac{T_{ref}}{T_{source} - 273.15}\right)^{1.048}\right]$, $f_{HE} = 0.4$	638.1	2018	[51]
MED_{S1}	$Z_{S1} = 0.16 \times Z_{MED}$	638.1	2018	[51]
MED_{S2}	$Z_{S2} = 0.16 \times Z_{MED}$	638.1	2018	[51]
MED_{S3}	$Z_{S3} = 0.16 \times Z_{MED}$	638.1	2018	[51]
MED_{S4}	$Z_{S4} = 0.16 \times Z_{MED}$	638.1	2018	[51]
MED_{S5}	$Z_{S5} = 0.16 \times Z_{MED}$	638.1	2018	[51]
MED_{S6}	$Z_{S6} = 0.16 \times Z_{MED}$	638.1	2018	[51]
MED Condenser	$Z_{MED.Cond} = 0.04 \times Z_{MED}$	638.1	2018	[51]

The Net Present Value (NPV) index serves as a tool to assess the economic reliability of the presented structure. It evaluates multiple points of view, comprising the payback period and the presented configuration's profitability at different steps of its economic lifetime. The primary goal of employing NPV is to determine whether the investment in the integrated configuration is economically justifiable over its operational lifetime. This is accomplished by regulating the net cash flow at each year's end to its current amount by pondering the interest rate [48]:

$$NPV_n = -TCI + \sum_{n=0}^{n} \frac{Y}{(1+i)^n} \tag{47}$$

$$Y = AI - \left(C^{O\&M} + C_f\right) \tag{48}$$

$$AI = c_{elec} \times t_{year} \times \dot{W}_{net} + c_{fw} \times t_{year} \times \dot{m}_{fw} + c_{H2} \times t_{year} \times \dot{m}_{H2} \tag{49}$$

$$C^{O\&M} = 0.06 \times Z_k \tag{50}$$

$$C_f = \dot{C}_4 \tag{51}$$

In these equations, AI, Y, and TCI denote the annual income, net flow of cash, and total capital investment, respectively. A positive NPV depicts that the configuration generates profit over its lifetime, while a negative NPV suggests economic infeasibility. Thus, including the NPV assess-

ment strengthens the study by complementing the thermodynamic and exergoeconomic evaluations with a comprehensive economic viewpoint.

The payback period term is expressed as the lowest period needed for the NPV to get positive values, and it is computable as follows [48]:

$$PP = \min\{n{:}NPV(n) > 0\} \tag{52}$$

The Sum Unit Cost of Product (SUCP) index is evaluated as [48]:

$$SUCP = \frac{\dot{C}_{w,net} + \dot{C}_{fw} + \dot{C}_{H2}}{\dot{W}_{net} + \dot{E}x_{65} + \dot{E}x_{69}} \tag{53}$$

3.3. The environmental viewpoint

Economic and thermodynamic evaluations alone are inadequate to fully capture the performance of a structure. It is also essential to ponder environmental factors, including toxicity, greenhouse gas emissions, pollution, and ozone layer depletion. To overcome these aspects, the exergoenvironmental balance equation and the definition of the exergoenvironmental impact rate ($\dot{B}$) are introduced through the following relations [52]:

$$\sum \dot{B}_{out,k} - \dot{Y}_k = \sum \dot{B}_{in,k} \tag{54}$$

$$\dot{B} = b \times \dot{E}x \tag{55}$$

Where b depicts the specific exergoenvironmental impact and $\dot{Y}_k$ symbolizes the environmental impact rate while neglecting exergetic impacts. The mentioned-above parameter is achievable as follows [52]:

$$\dot{Y}_k = \frac{Y_k}{n \times HR} \tag{56}$$

$$Y_k = \sum_i \omega_{i,k} \times M_{i,k} \tag{57}$$

Where, Y_k depicts the environmental impact. $M_{i,k}$ exhibits the component mass, and $\omega_{i,k}$ illustrates the eco-99 coefficient, which is different according to the component type. Furthermore, the subscript i depicts the material type utilized in the manufacturing of the components.

For heat transfer components, evaporators, mixers, and condensers, the M_k can be achieved by the following equation, which considers the Thickness (δ), the employed material's density (ρ), and surface area (A_k) [52]:

$$M_k = \rho \times A_k \times \delta \tag{58}$$

Besides, this parameter is accountable for turbines, pumps, and compressors as expressed in the following equation [52]:

$$M_k = \alpha_k \times \dot{W}_k \tag{59}$$

In which α_k is describable as the specific mass, as reported in Ref. [53].

For the presented study, the value of the product's exergoenvironmental impact rate ($\dot{B}_{P,tot}$) can be achieved as follows:

$$\dot{B}_{P,tot} = \dot{B}_{SOFC} + \dot{B}_{ST} + \dot{B}_{65} + \dot{B}_{69} \tag{60}$$

According to the aforementioned explanations, the thermal and exergetic efficiencies of the presented structure are expressed as:

$$\eta_{thermal} = \frac{\dot{W}_{net} + \dot{H}_{65} + LHV^{PEM}_{H_2}}{LHV_{CH_4} \times \dot{m}_{CH_4}} \times 100 \tag{61}$$

$$\eta_{exergy} = \frac{\dot{W}_{net} + \dot{E}x_{65} + \dot{E}x_{69}}{\dot{E}x_4} \times 100 \tag{62}$$

3.4. The optimization procedure

The Particle Swarm Optimization (PSO) algorithm is utilized to support the administration of favourable multi-criteria optimization assignments. PSO is a population-based approach, where each component, defined as particles, collaboratively forms swarms. Every single particle traverses an established solution zone, with its velocity and position being persistently tracked during the optimization procedure. The main purpose is to locate the optimal location inside the swarm to maximize the purpose of the objective. This includes the assessment of several objective functions and the evaluation of their corresponding fitness levels. Following this assessment, the particles' positions and velocities are regulated based on the subsequent equations [54]:

$$X_{id}^{(t+1)} = X_{id}^{(t)} + V_{id}^{(t+1)}, i = 1, 2, \ldots, N_{p,d} = 1, 2, \ldots, N_d \tag{63}$$

$$V_{id}^{(t+1)} = V_{id}^{(t)} + C_1 r_1 \left[P_{id}^{(t)} - X_{id}^{(t)}\right] + + C_2 r_2 \left[P_{gd}^{(t)} - X_{id}^{(t)}\right] \tag{64}$$

Herein N_{max} represents the iterations' maximum number, N_p signifies the solutions count, and N_d signifies the involved number of dimensions. Furthermore, r and C are crucial factors in which C symbolizes the acceleration index, and r refers to a numerical index. Both factors are restricted in the [0,1] range. The iterative procedure is repeated until the mentioned variables reach a stable state. Throughout the repetitions, the algorithm seeks a broad spectrum of potential optimal conditions, which collectively form the Pareto front curve. The ultimate optimal state is then determined from this Pareto frontier.

The optimization procedure considers the freshwater production rate ($\dot{m}_{fw}$), SUCP, and exergy efficiency (η_{ex}) as the cost functions, which are optimized through two scenarios. The selected variables are the reforming temperature (T_{SMR}), air compressor's pressure ratio (PR_{AC}), steam to methane ratio (SCR), SOFC's current density (J), stack flow temperature (T_{stack}), and fuel utilization factor (U_f). These variables' variation domains are illustrated in Table 2.

4. Results and analysis

In this section, the simulation process's outcomes are illustrated in terms of validation, baseline results, sensitivity analysis, and optimization results.

4.1. The validation process

Since the current investigation relies on numerical analysis, ensuring the accuracy of the simulation process is crucial. To this end, the SMR, SOFC, MED, and PEME units are validated using similar references. It's important to note that the validation process utilizes data from these references as input. The SMR unit is validated using data from Sadeghi et al. [38], where the molar fractions of the products are compared and summarized in Table 3. The SOFC unit's modeling is verified with data from Tao et al. [55], where the voltage of the fuel cells is estimated and compared under various current densities, as shown in Table 4. The validation of the MED unit's modeling is performed using data from Hamrang et al. [56], comparing parameters such as freshwater

Table 2
The optimization process's variables and associated variation domains.

Variable	Variation domain
T_{SMR}	550 – 650 [℃]
PR_{AC}	2.5 – 3.5
SCR	1.5 – 2.5
J	7000 – 8500 [A /m^2]
T_{stack}	750 – 800 [℃]
U_f	0.8 – 0.9

Table 3
The SMR validation with Sadeghi et al. [38].

Substances	Estimated value [%]	Reference value [%]	Error [%]
CH_4	16.09	16.15	0.81
H_2	38.15	38.02	0.34
CO	3.23	3.21	0.62
CO_2	7.11	7.09	0.28
Operating Conditions			
Steam to methane molar ratio in the reformer			2
Mass flow of Methane			0.16 [kg/s]
Reformer temperature			1300 [K]
Pressure of the reformer			394.6 [kPa]

Table 4
The SOFC verification with Tao et al. [55].

Current density [A/m^2]	Estimated Voltage [V]	Reference Voltage [V]	Error [%]
6000	0.51	0.52	0.61
5000	0.59	0.57	3.23
4000	0.65	0.63	2.47
3000	0.69	0.68	2.03
2000	0.74	0.76	2.86
1000	0.80	0.85	5.48
Operating Conditions			
The temperature difference between the SOFC inlet and outlet			100 [K]
Base inlet temperature to the SOFC			1000 [K]
Fuel utilization factor			0.85
Steam to carbon ratio			2.5

production rate, brine flow salinity, and operating pressure of the first stage, as presented in Table 5. Finally, the PEME unit's validation is based on data from Ioroi et al. [57], where cell voltages are evaluated and compared, as shown in Table 6. The obtained error values indicate acceptable accuracy in the simulation process, thereby validating the outputs outlined in the subsequent sections.

4.2. The baseline results

This section presents the baseline findings using the information from Table 7. These results encompass overall performance, economic analysis, and exergy analysis. The thermophysical and economic properties of the streamlines are summarized in Table S.3 of the supplementary file, yielding a net power production of 1039 kW, a freshwater rate of 0.88 kg/s, and a hydrogen rate of 0.00175 kg/s. These values correspond to energy and exergy efficiencies of 33.28 % and 26.87 %, respectively. In addition, the SUCP and payback period are estimated to be approximately 21.10 $/GJ and 5.73 years.

4.2.1. The exergy analysis

In Fig. 2, the exergy flow within the configuration is depicted in the form of a Sankey diagram. Methane initially carries a 4869-kW exergy rate, which rises to 5140 kW at the reformer's inlet. The SOFC's anode is supplied with an input exergy rate of 6433 kW, while the cathode intake

Table 5
Verification of the MED unit with Hamrang et al. [56].

Parameter	Estimated	Reference	Error [%]
The brine flow salinity [g/kg]	55	55.91	1.62
Rate of water production [kg/s]	0.8223	0.8311	1.034
First stage operating pressure [bar]	0.275	0.265	3.78
Operating Conditions			
Seawater mass flow rate			20 [m^3/h]
Seawater temperature increment in each preheater			2.3 [°C]
MED final-stage temperature			321.15 [K]

Table 6
The PEME verification with similar work by Ioroi et al. [57].

Current density [A/m^2]	Estimated Voltage [V]	Reference Voltage [V]	Error [%]
200	1.67	1.7	1.7
400	1.74	1.76	0.82
1000	1.83	1.83	0.22
1500	1.872	1.87	0.12
3000	1.93	1.92	0.71
4000	1.98	1.96	1.4
5000	2.042	2	2.1
Operating Conditions			
Operating temperature			80 [°C]
Operating pressure			0.30 [MPa]

Table 7
The simulation process inputs data for the baseline operating mode.

Parameter	Value	Parameter	Value
Reference temperature, T_0 [°C]	25	Reformer Temperature, T_{SMR} [°C]	600
Reference pressure, P_0 [kPa]	101.3	Outlet temperature of HX2 [°C]	500
AC pressure ratio, PR_{AC} [−]	3	Outlet temperature of HX3 [°C]	400
Temperature difference in stack, ΔT_{stack} [°C]	100	Cooling water temperature [°C]	25
Number of fuel cells, N_{cells} [−]	50000	Seawater salinity, [g/kg]	42
Baseline current density, J [A/m^2]	8000	Temperature of the MED feed water, $T_{fw,MED}$ [°C]	35
Exchange current density of cathode, J_c [A/m^2]	2500	Temperature difference between effects , ΔT_{eff} [°C]	4.8
Exchange current density of anode, J_a [A/m^2]	6500	Temperature of the top brine [°C]	95
Effective gaseous diffusivity of cathode [cm^2/s]	0.05	Working Temperature of PEM [°C]	80
Effective gaseous diffusivity of anode [cm^2/s]	0.2	Bottom sea water salinity [g/kg]	70
Anode thickness, L_{anode} [mm]	0.5	Pressure of oxygen, P_{O_2} [kPa]	101.3
Cathode thickness, $L_{cathode}$ [mm]	0.05	The pressure of hydrogen, P_{H_2} [kPa]	101.3
Electrolyte thickness, $L_{electrolyte}$ [mm]	0.01	Faraday constant, F [C/mol]	96486
Interconnect thickness, $L_{interconnect}$ [mm]	3	The anode-side water content, λ_a [1 / Ω]	14
Anode & cathode recycling ratio, R [%]	40	The cathode-side water content, λ_c [1 / Ω]	10
Fuel utilization ratio, U_f [−]	0.85	The thickness of the membrane, L [μm]	100
Higher pressure of ST [kPa]	600	Pre-exponential anode factor, j_a^{ref} [A/m^2]	170000
Middle pressure of ST [kPa]	200	Pre-exponential cathode factor, j_c^{ref} [A/m^2]	4600
Lower pressure of ST [kPa]	10	Cathode's activation energy, $E_{act,c}$ [kJ/mol]	18
Isentropic efficiency of Pu, $\eta_{is,pu}$ [%]	70	Energy of activation of the anode, $E_{act,a}$ [kJ/mol]	76
Isentropic efficiency of ST, $\eta_{is,ST}$ [%]	85		

stream contains an exergy rate of 7177 kW, resulting in 2354 kW of power generation in the SOFC. The electrolysis process through the SOFC leads to a 498-kW exergy destruction rate, while the combustion process within the AB corresponds to an exergy destruction rate of 474 kW. These components represent the primary sources of irreversibility. The exergy rate carried by the stack flow is 5980 kW, which decreases to 877 kW at the stack. In the steam Rankine cycle, the steam turbine possesses a 564-kW energy rate, resulting in power generation of 366

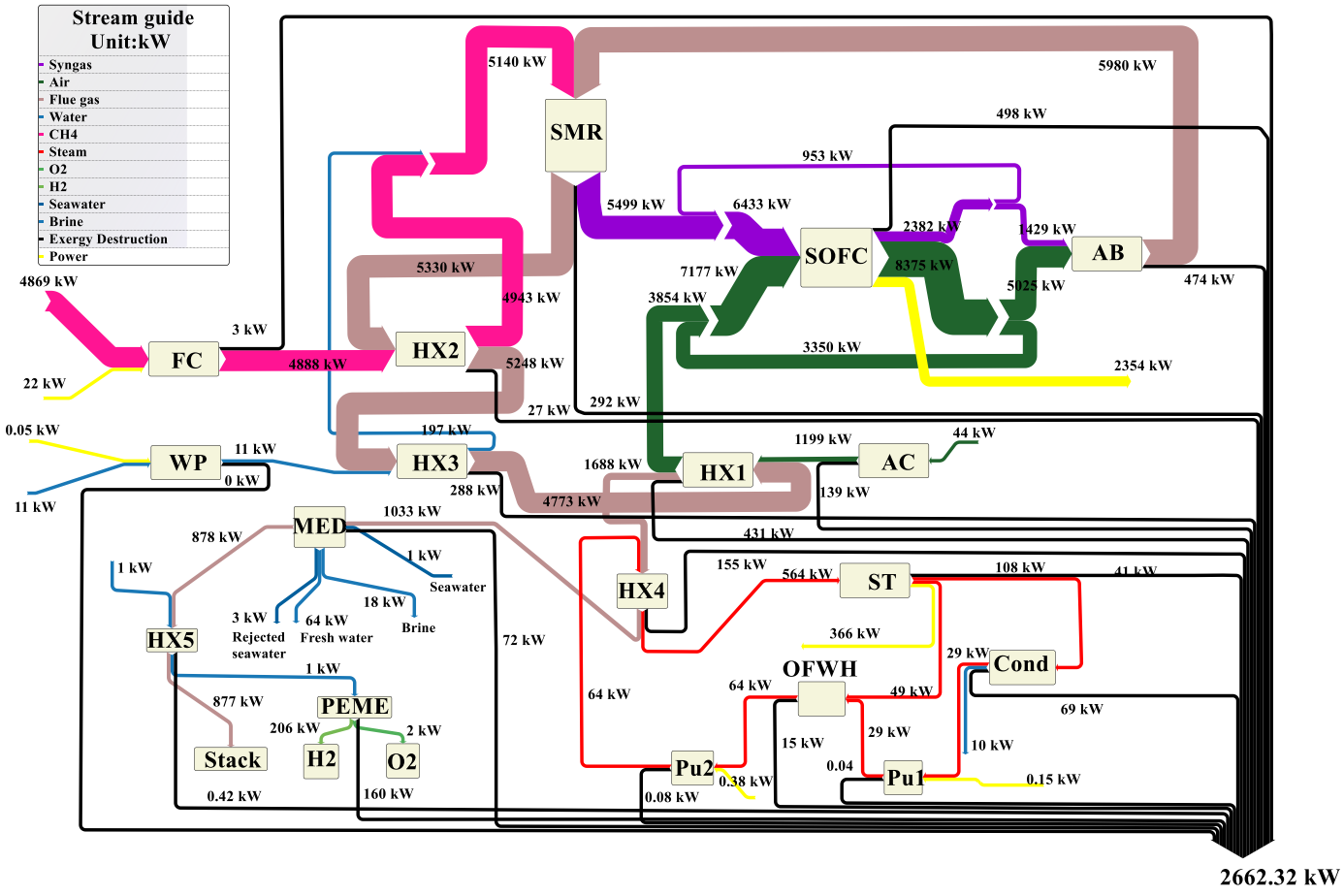

Fig. 2. The designed configuration's Sankey diagram.

kW and a rate of 41 kW for exergy destruction within the turbine. Furthermore, the MED unit contributes to a 72-kW exergy destruction rate, while the PEME unit's exergy destruction rate is 160 kW. Ultimately, the total exergy destruction rate of the designed configuration is estimated to be approximately 3662.32 kW.

4.2.2. *The economic analysis*

The analysis of the economy aims to evaluate the per exergy unit cost within the components, the cost rate related to exergy destruction ($\dot{C}_D$), total cost rate ($\dot{Z}_k$), components' purchase cost, and the economic feasibility under different economic scenarios. Table 8 indicates the per exergy unit cost of each component's fuel ($c_{F,k}$) and product ($c_{P,k}$) streams, cost rate related to exergy destruction, and total cost rate. Referring to this Table, although the SOFC corresponds to the highest exergy destruction, the $\dot{C}_D$ of the AB and HX1, with values of 132764.06 $/year and 132746.28 $/year, respectively, are higher than that of the SOFC. Additionally, the steam turbine has a $\dot{C}_D$ of 19334.2 $/year, which is considerable given its exergy destruction rate (40.63 kW). The steam turbine and SOFC contribute the highest $\dot{Z}_k$ among the components, with values of 239591.65 $/year and 109050.25 $/year, respectively.

Fig. 3 illustrates the distribution of components' purchase costs within the total capital investment cost. The SOFC, steam turbine (ST), and PEME account for the highest purchase costs, valued at 1.047, 0.477, and 0.366 $M, respectively. These values correspond to shares of 38.09 %, 17.33 %, and 13.32 %, respectively, in the total capital investment cost. The SOFC unit, comprising the reforming process, fuel cells, and AB, represents the largest portion of the total capital investment cost, with a share of 64.52 %. In comparison, the steam Rankine cycle contributes a 21.88 % share of the overall investment.

Table 8
The components' economic analysis outcomes.

Components	$c_{F,k}$ [$/GJ]	$c_{P,k}$ [$/GJ]	$\dot{C}_D$ [$/year]	$\dot{Z}_k$ [$/year]
AB	279.94	308.29	132764.06	36764.62
AC	279.94	374.25	38856.41	70065.37
Cond	475.9	4457.84	32756.3	7137.06
FC	279.94	574.35	699.76	4949.03
HX1	308.29	360.1	132748.28	4805.98
HX2	308.29	463.56	8430.65	92.43
HX3	308.29	785.55	88867.24	325.16
HX4	308.29	419.31	47752.3	7745.06
HX5	308.29	740.51	128.37	37.9
MED Condenser	259.39	1691.3	4830.2	55.59
MED_{S1}	308.29	404.53	11221.09	222.37
MED_{S2}	367.54	370.62	75.45	222.37
MED_{S3}	326.32	336.91	588.08	222.37
MED_{S4}	286.54	306.78	957.58	222.37
MED_{S5}	253.04	287.33	1215.41	222.37
MED_{S6}	235.75	296.83	1451.2	222.37
OFWH	479.03	911.57	6946.92	20680.04
PEME	279.89	899.67	44757.91	83813.64
Pu1	279.94	2756.29	11.76	255.27
Pu2	279.94	2051.3	23.91	490.18
SMR	308.29	675.46	89859.28	41633.61
SOFC	252.08	279.94	125639.16	239591.65
ST	475.9	826.4	19334.2	109050.25
WP	279.94	3054.87	2.18	120.25

Fig. 4 illustrates the NPV and PP metrics of the designed configuration for different methane purchase costs and electricity sale costs. The configuration needs a capital investment cost of 2.75 $M, with the PP

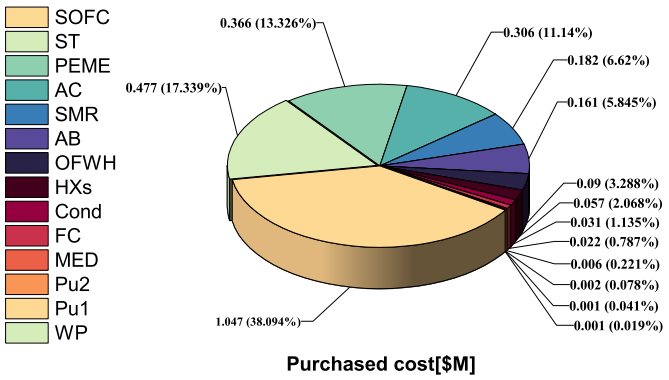

Fig. 3. The distribution of the purchase cost within the components.

and NPV values shown for methane purchase costs of 2, 2.5, and 3.365 $/GJ in Fig. 4a. As expected, the PP increases and NPV decreases with an increment in the methane purchase cost. The metrics' values exhibit a PP of 4.32 years for 2 $/GJ, 4.75 years for 2.5 $/GJ, and 5.74 years for 3.365 $/GJ. The associated NPV values for these purchase costs are approximately 2.95 $M, 2.58 $M, and 1.94 $M at the end of the configuration's lifetime.

Fig. 4b presents the PP and NPV metrics for electricity selling costs of 0.14, 0.16, and 0.18 $/kWh. The PP decreases with an increase in the electricity sale cost, while the NPV metrics rise. Therefore, the PP for an electricity selling cost of 0.14 $/kWh is approximately 5.74 years, while for costs of 0.16 and 0.18 $/kWh, the PP values are 4.44 years and 3.63 years, respectively. The associated NPV values for these costs are approximately 1.94 $M, 2.85 $M, and 3.76 $M, respectively.

4.2.3. The environmental analysis

The performance of the presented structure is also assessed from the environmental aspect, where an exergoenvironmental impact rate of 14.48 Pt/h is achieved. Besides, the exergoenvironmental outputs associated with each state of the presented structure and also its components are added in Tables 9 and 10.

4.3. The sensitivity analysis

In this section, a sensitivity analysis is conducted to study the effect of T_{SMR}, SCR, PR_{AC}, J, T_{stack}, and U_f on the performance metrics. The investigated performance metrics comprise the net power production ($\dot{W}_{net}$), freshwater production rate ($\dot{m}_{fw}$), hydrogen production rate ($\dot{m}_{H2}$), SUCP, and η_{ex}.

4.3.1. The reforming temperature

Fig. 5 demonstrates the influence of a change in T_{SMR} on performance metrics, ranging from 550 to 650 °C. As T_{SMR} increases, more input heat is required for the reforming process, supplied by the stack flow. In terms of the SMR's energy balance, the intake streams of methane and water are reduced. However, hydrogen production within the reforming process increases, necessitating more intake of air to the SOFC. Consequently, SOFC power generation drops due to the reduced fuel mass flow rate, while the stack flow carries a higher energy level. This leads to an elevation in the input energy for the steam Rankine cycle and MED subsystems, resulting in increased freshwater production, power generation, and PEME input power. The higher PEME input power contributes to an increased hydrogen production rate. However, the exergetic efficiency exhibits a downward behavior, while the SUCP rises because of the decreased net power generation. Finally, the amounts of $\dot{B}_{P,tot}$ confront an increment with the growth of T_{SMR} in this specified range.

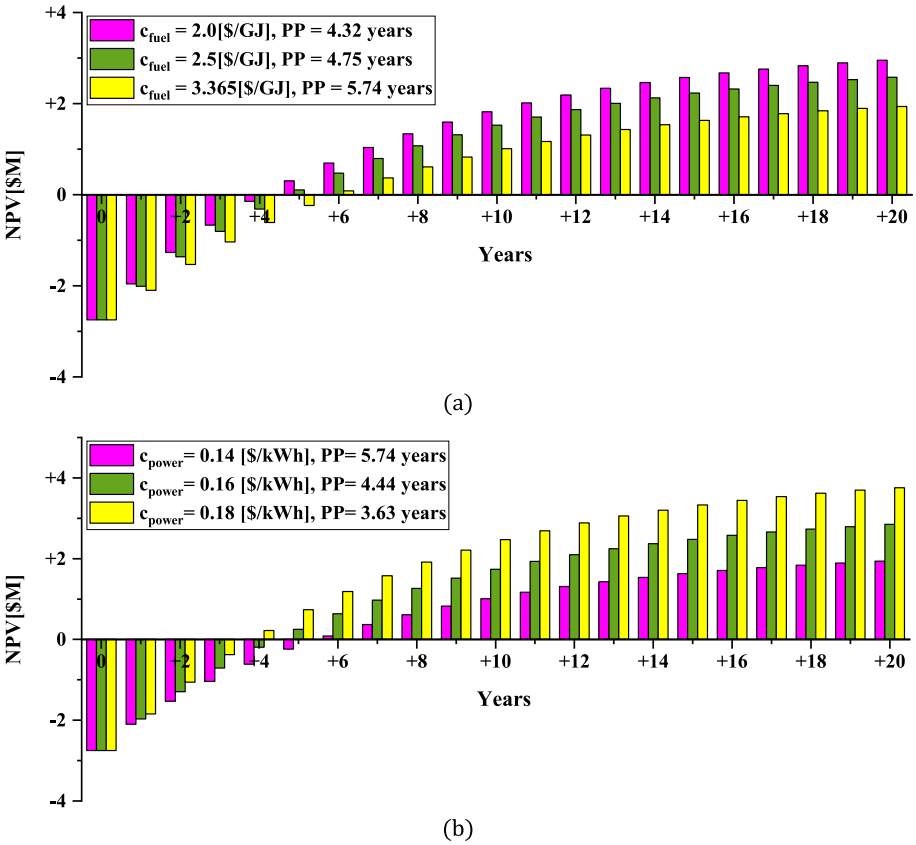

Fig. 4. The PP and NPV metrics for different economic scenarios.

Table 9
The exergoenvironmental outputs associated with each state of the presented structure.

States	b_k [pts /GJ]	$\dot{B}$ [pts /h]	States	b_k [pts /GJ]	$\dot{B}$ [pts /h]
1	0.00	0.00	36	1.28	4.05
2	0.01	0.00	37	0.00	0.00
3	3.09	2.20	38	5.78	0.08
4	0.70	12.24	39	5.78	0.05
5	0.70	12.34	40	5.78	0.03
6	0.71	12.72	41	5.78	0.01
7	0.81	14.91	42	5.78	0.01
8	0.91	17.92	43	5.78	0.01
9	0.95	22.00	44	5.78	0.01
10	1.19	10.20	45	5.78	0.01
11	1.19	4.08	46	5.78	0.01
12	1.19	6.12	47	1.53	0.63
13	0.00	0.00	48	5.78	0.09
14	1.28	5.54	49	1.53	0.10
15	1.43	19.80	50	1.36	0.46
16	1.32	34.15	51	5.78	0.17
17	1.19	35.87	52	1.36	0.07
18	1.19	14.35	53	1.20	0.32
19	1.19	21.52	54	5.78	0.25
20	1.28	27.64	55	1.20	0.05
21	1.28	24.64	56	1.05	0.21
22	1.28	24.26	57	5.78	0.31
23	1.28	22.06	58	1.05	0.03
24	1.28	7.80	59	0.97	0.14
25	1.28	4.78	60	5.78	0.35
26	2.13	0.49	61	0.97	0.02
27	2.13	0.49	62	1.04	0.10
28	1.73	3.52	63	5.78	0.37
29	1.73	0.31	64	1.04	0.02
30	1.73	0.67	65	1.28	0.29
31	1.73	0.18	66	0.00	0.00
32	1.73	0.18	67	0.95	0.00
33	0.00	0.00	68	2.11	0.01
34	0.05	0.49	69	2.11	1.56
35	1.28	4.06			

Table 10
The fuel, product, and destruct-related specific exergoenvironmental impact for the components of the presented study.

Components	$b_{F,k}$ [pts /GJ]	$b_{P,k}$ [pts /GJ]	$\dot{B}_D$ [pts /h]
AB	1.19	1.28	2.03
AC	1.19	1.33	0.59
Cond	1.73	13.66	0.43
FC	1.19	1.35	0.01
HX1	1.28	1.49	1.99
HX2	1.28	1.92	0.13
HX3	1.28	3.27	1.33
HX4	1.28	1.68	0.72
HX5	1.28	2.68	0.00
MED-Cond	1.04	6.74	0.07
MED_S1	1.28	1.68	0.17
MED_S2	1.53	1.54	0.00
MED_S3	1.36	1.40	0.01
MED_S4	1.20	1.27	0.01
MED_S5	1.05	1.18	0.02
MED_S6	0.97	1.19	0.02
PEME	1.19	2.11	0.68
Pu1	1.19	1.66	0.00
Pu2	1.19	1.54	0.00
SMR	1.28	2.33	1.35
SOFC	1.15	1.19	2.06
ST	1.73	1.93	0.25
WP	1.19	1.40	0.00

In this scenario, terms $\dot{W}_{net}$ and η_{ex} decrease from about 1173 to 814.6 kW and 29.61 to 22.51 %, respectively. Meanwhile, the $\dot{m}_{fw}$, $\dot{m}_{H2}$, SUCP, and $\dot{B}_{P,tot}$ increase within the ranges of 0.80–0.99 kg/s, 0.00176–0.00184 kg/s, 18.97–24.91 $/GJ, and 14.16–15 Pt/h, respectively.

4.3.2. The steam-to-methane ratio

The impact of SCR on the functional metrics is shown in Fig. 6, in which this term varies within a range of 1.5–2.5. An increase in the steam ratio within the reformer requires a higher heat transfer rate, leading to a reduction in the intake of fuel. Thus, the anode is fed by a lower intake syngas rate, which decreases the SOFC's power generation. Despite the boiler intake stream (state 24) carrying a higher energy level and elevating the steam Rankine cycle's input energy, more steam is extracted from the high-pressure section steam turbine. This matter reduces the steam turbine's overall power generation and PEME input power. Subsequently, the hydrogen production rate witnesses a reduction. While the MED's input heat increases in the first stage, and improves the freshwater production. The exergetic efficiency and SUCP metrics are mainly influenced by power generation, leading to a reduction in efficiency and an increase in the SUCP. Besides, the values of $\dot{B}_{P,tot}$ act similarly to the SUCP so that, increases with the growth of SCR values. In this regard, terms $\dot{W}_{net}$, $\dot{m}_{H2}$, and η_{ex} decrease within the ranges of 1137-949.7 kW, 0.00195–0.00163 kg/s, and 29.13–24.90 %, respectively. Also, terms $\dot{m}_{fw}$, SUCP, and $\dot{B}_{P,tot}$ increase from 0.81 to 0.94 kg/s, 20.43 to 21.63 $/GJ, and 12 to 17 Pt/h.

4.3.3. The air compressor pressure ratio

Fig. 7 shows the PR_{AC} variation impact on the performance metrics in a span of 2.5–3.5. An increase in PR_{AC} rises the cathode's operating pressure and requires a higher anode's operating pressure. Hence, the FC and AC consume more power, and streams 5 and 2 carry a higher energy level. Pondering the HXs 2 and 3 energy balance, the intake fuel and water rates are reduced. This matter reduces the SOFC's power generation. However, stream 14 carries a higher temperature due to its elevated pressure, and stream 24 leaves HX1 with a higher temperature. Subsequently, the steam Rankine cycle's input energy rises and improves its power generation, increasing the PEME input power. Despite of increased temperature of stream 25, the reduced mass flow rate has a higher impact on the MED's input heat, resulting in a lower heat transfer rate within the MED's first stage and reducing the freshwater production rate. The exergetic efficiency and SUCP metrics are mainly affected by power generation, leading to a reduction in efficiency and an increase in the SUCP. Furthermore, the amounts of $\dot{B}_{P,tot}$ raise with the increment of PR_{AC} in the specified range.

In summary, terms $\dot{W}_{net}$, $\dot{m}_{fw}$, and η_{ex} decrease within the ranges of 1196-900.4 kW, 0.94–0.83 kg/s, and 29.58–24.56 %, respectively. Also, terms $\dot{m}_{H2}$, SUCP, and $\dot{B}_{P,tot}$ increase from 0.0015 to 0.0020 kg/s, 19.61 to 22.82 $/GJ, and 14.36 to 14.66 Pt/h.

4.3.4. The current density

Fig. 8 shows the performance behavior to a change in J within a range of 7000–8500 A/m^2. An escalation in the SOFC's current density heightens the removal of heat from the cells, leading to an increase in ohmic resistance and voltage. This surge in the ohmic voltage subsequently diminishes the overall voltage and power generation within the fuel cells. However, the augmented removal of heat from the SOFC amplifies the input heat required by the subsystems, thereby boosting power generation in the steam Rankine cycle, hydrogen production in the PEME, and freshwater production in the MED. Despite the enhancements in hydrogen and freshwater production, the exergetic efficiency, SUCP, and $\dot{B}_{P,tot}$ are primarily influenced by power generation. Consequently, the decreased net power generation leads to a reduction in exergy efficiency, and an increase in SUCP and $\dot{B}_{P,tot}$ values. In this way, terms $\dot{W}_{net}$ and η_{ex} decrease within the ranges of 1056-1015 kW and 30.05–25.36 %. Also, terms $\dot{m}_{H2}$, $\dot{m}_{fw}$, SUCP, and $\dot{B}_{P,tot}$ increase from 0.00145 to 0.00195 kg/s, 0.73–0.96 kg/s, 19.99 to 21.78 $/GJ, and 11 to 16.5 Pt/h respectively.

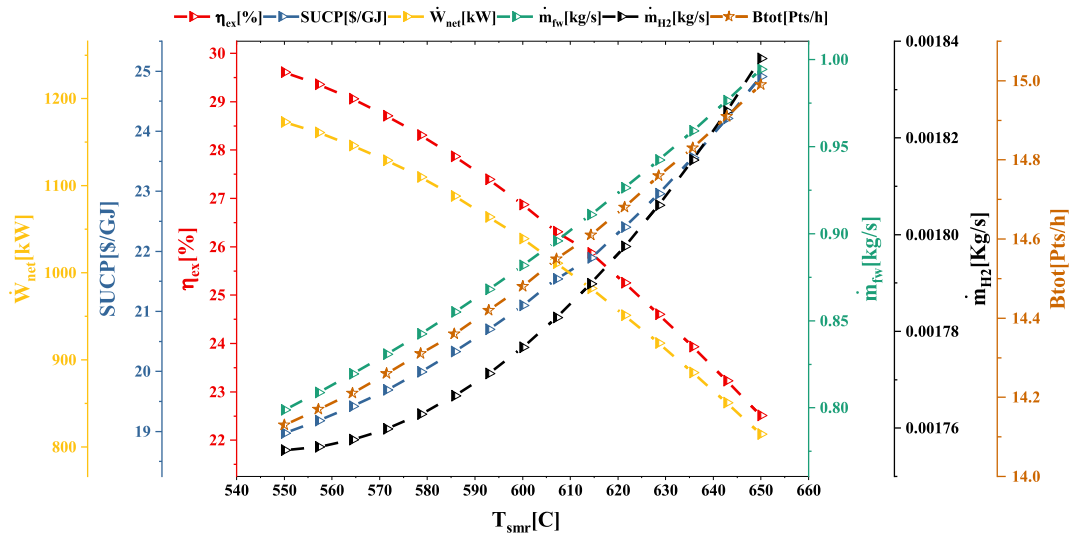

Fig. 5. The reforming temperature's impact on the performance metrics.

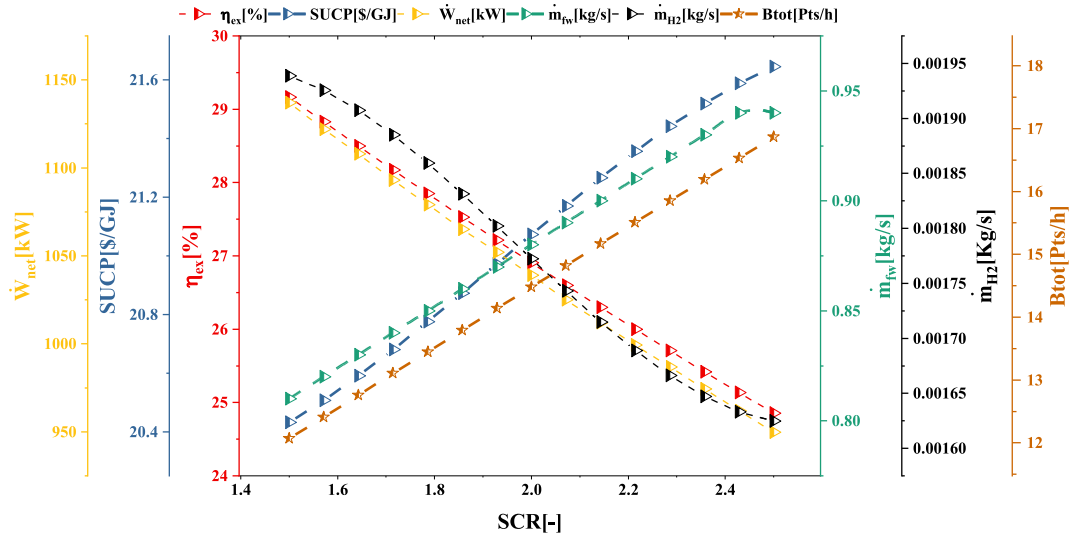

Fig. 6. The steam-to-methane ratio's impact on the performance metrics.

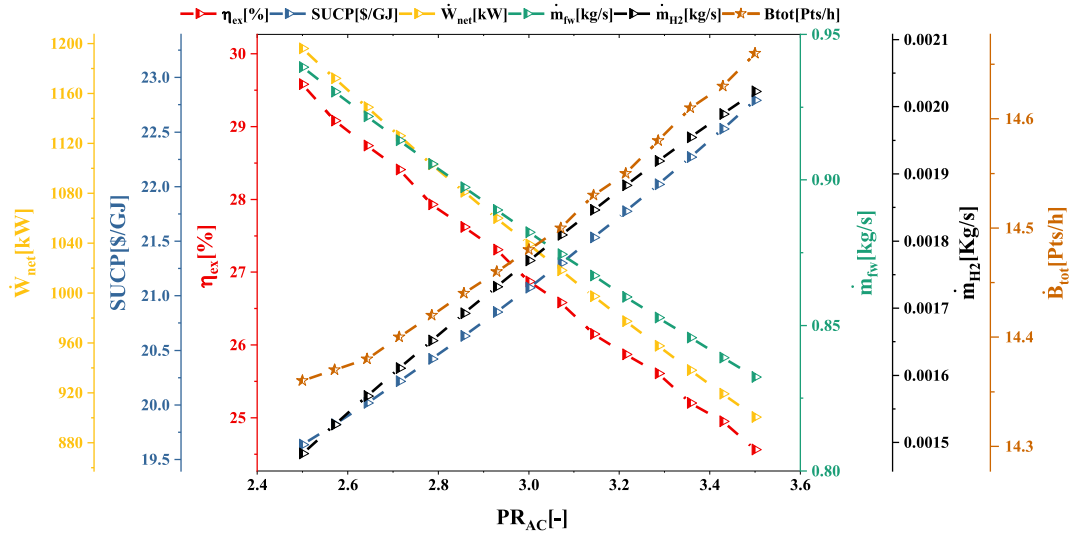

Fig. 7. The air compressor's pressure ratio impact on the performance metrics.

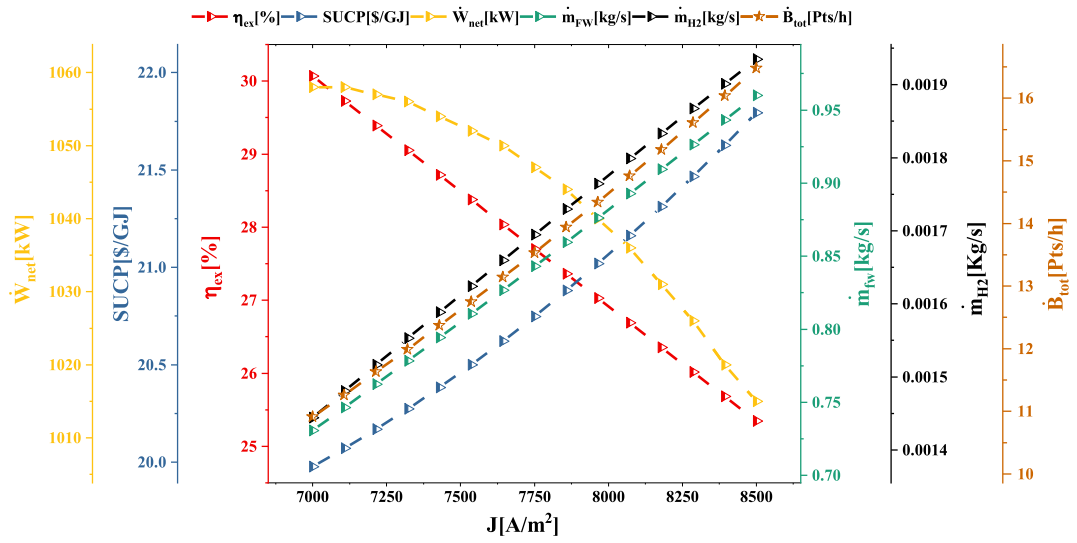

Fig. 8. The SOFC current density impact on the performance metrics.

4.3.5. *The fuel utilization factor*

The effect of U_f on the functional metrics is depicted in Fig. 9, with this parameter's influence examined within a range of 0.8–0.9. An elevation in U_f raises the SOFC's operating temperature, consequently increasing the ohmic resistance within the fuel cells and diminishing power generation. This scenario necessitates more intake of air to the cathode, escalating the AC's power consumption. However, the feed stream rates to the AB decrease, although they carry higher temperatures. Consequently, the stack flow exhibits a lower mass flow rate but at a higher temperature. The mass flow rate of the steam Rankine cycle reduces due to the boiler's energy balance and the decreased stack flow rate, while the heat transfer rate within the MED's first stage is affected by the stack flow's higher temperature. Consequently, the hydrogen production rate declines owing to the decreased input power to the PEME, whereas freshwater production increases due to the improved heat transfer rate within the MED's first stage. The exergy efficiency, $\dot{B}_{P,tot}$, and SUCP are primarily influenced by net power production. Consequently, the exergy efficiency and $\dot{B}_{P,tot}$ decrease, while SUCP increases as a result of the U_f variation. In this regard, terms $\dot{W}_{net}$, $\dot{m}_{H2}$, η_{ex}, and $\dot{B}_{P,tot}$ decrease within the ranges of 1148-737.6 kW, 0.00192–0.00176 kg/s, 28.60–21.77 %, and 15.51 to 13.7 Pt/h, respectively. Also, $\dot{m}_{fw}$ and SUCP increase from 0.84 to 0.98 kg/s and from 20.18 to 24.78 $/GJ.

4.3.6. *The stack flow temperature*

The effect of T_{stack} on the performance metrics is represented in Fig. 10, varying in a span of 750–800 °C. An increment in T_{stack} reduces the intake of air and fuel rates to the SOFC, which results from the AB's energy balance. The impact of higher temperature in the stack flow improves the heat transfer rate within SMR and HXs 1, 2, 3, and the boiler. Subsequently, the hydrogen fraction within the syngas composition increases, resulting in an increment in the SOFC's power generation. Also, more steam is generated within the boiler to feed the steam turbine, leading to an increase in this unit's power generation and PEME's input power. However, the reduced mass flow rate of stack flow impact is signified within the MED's first stage energy balance, in which the heat transfer rate reduces and lower saline water evaporates. So, hydrogen production witnesses an increase, while freshwater production declines. The exergy efficiency depicts an upward behavior, while the SUCP and $\dot{B}_{P,tot}$ perform a downward trend due to increased net power production. In this regard, terms $\dot{W}_{net}$, $\dot{m}_{H2}$, and η_{ex} elevate from 713 to 1090 kW, 0.00165–0.00182 kg/s, and 20.34–27.98 %,

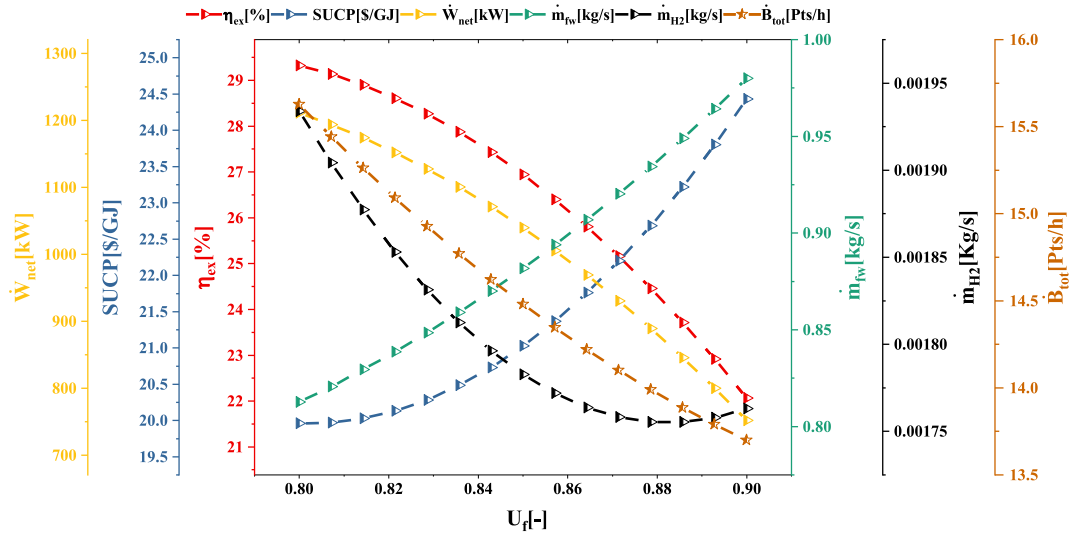

Fig. 9. The fuel utilization impact in the performance metrics.

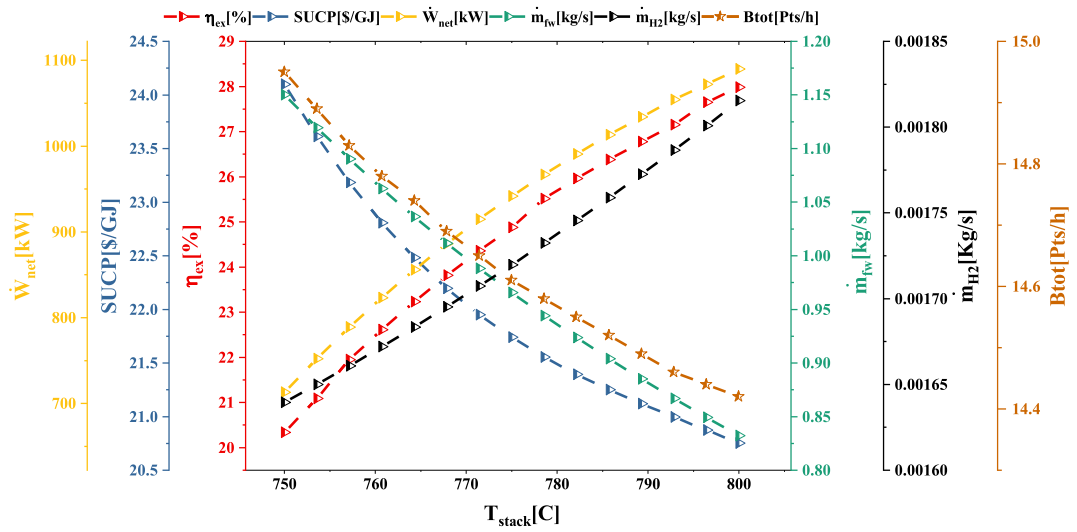

Fig. 10. The stack flow temperature's impact on the performance metrics.

respectively. Also, terms $\dot{m}_{fw}$, SUCP, and $\dot{B}_{P,tot}$ decrease from 1.15 to 0.83 kg/s, 24.11 to 20.77 $/GJ, and 14.95 to 14.41 Pt/h, respectively.

4.4. The optimization outcomes

As mentioned, the optimization procedure focuses on the functions $\dot{m}_{fw}$, SUCP, and η_{ex}, which are optimized through two scenarios. In the first scenario, the goal is to maximize $\dot{m}_{fw}$, while minimizing SUCP, whereas in the second scenario, both $\dot{m}_{fw}$ and η_{ex} are maximized. The outcomes of these scenarios are represented in terms of a Pareto frontier, and the LINMAP method selects the optimal state. Fig. 11 displays the results of the first scenario, where the optimal state yields $\dot{m}_{fw}$ of 0.95 kg/s with an associated SUCP of 18.33 $/GJ. On the other hand, Fig. 12 illustrates the outcomes of the second scenario, where the optimal $\dot{m}_{fw}$ and η_{ex} are approximately 0.98 kg/s and 28.46 %, respectively.

The final optimal operating mode is determined by comparing the operational metrics of the baseline and optimal conditions, as shown in Table 11. The results indicate improvements in all metrics compared to the baseline, except for $\dot{m}_{H2}$, which decreases to 0.0016 kg/s in both optimal scenarios. The power production in the first scenario is 1201.58 kW, while in the second scenario, it increases to approximately 1221.76 kW. Moreover, the second scenario brings out a higher freshwater production rate of 0.98 kg/s compared to 0.95 kg/s in the first scenario. However, the first scenario exhibits higher thermal and exergy efficiency due to its lower intake of fuel. From an economic standpoint, the first scenario demonstrates better performance in terms of both SUCP and PP despite the higher product rate in the second scenario. The

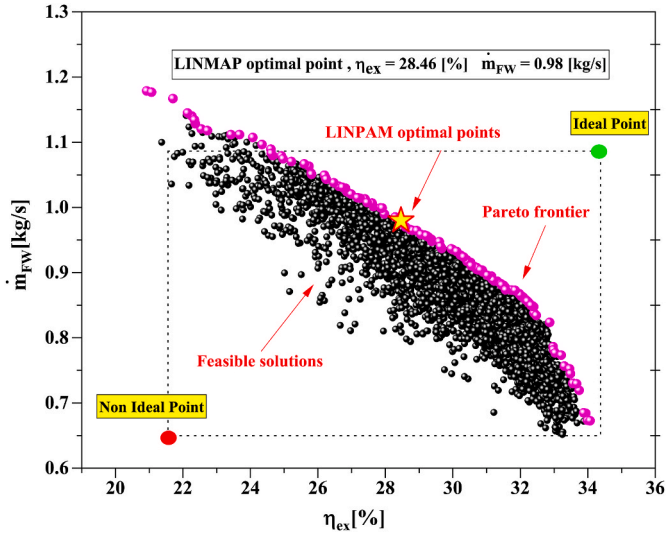

Fig. 12. The second scenario's outcomes.

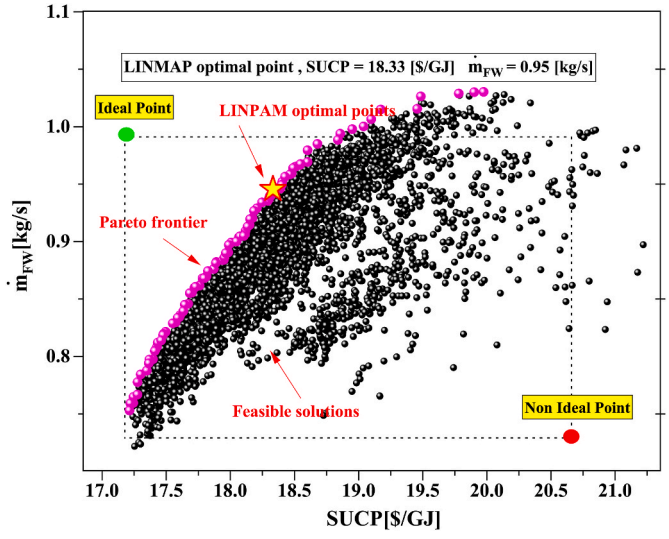

Fig. 11. The first scenario's results.

Table 11
The contrast of the baseline and optimal approaches' performance metrics.

Parameter	Unit	Base design	$SUCP - \dot{m}_{fw}$	$\eta_{ex} - \dot{m}_{fw}$
Net output power, $\dot{W}_{net}$	[kW]	1039.0	1201.58	1221.76
Exergy efficiency, η_{ex}	[%]	26.87	29.86	28.46
Energy efficiency, η_{th}	[%]	33.28	36.73	35.54
Mass flow rate of fresh water, $\dot{m}_{fw}$	[kg/s]	0.88	0.95	0.98
Rate of produced Hydrogen, $\dot{m}_{H2}$	[kg/s]	0.00175	0.0016	0.0016
Payback period	[Year]	5.73	3.63	4.6
SUCP	[$/GJ]	21.10	18.33	19.89
The product's exergoenvironmental impact rate, $\dot{B}_{P,tot}$	[Pts/h]	14.48	13.92	13.46

higher product rate in the second scenario leads to a higher purchase cost of the SOFC, which contributes 38.09 % of the capital investment cost. In addition, the lower SUCP in the first scenario indicates that this scenario generates higher profit from product sales.

In the final step, the outputs of the presented structure are compared with a similar work in the literature to prove this structure's advantage. Thus, a similar work by Bicer and Dincer [58] is considered for comparisons, and the results are depicted in Fig. 13. The present assessment integrates SOFC, SMR, PEME, MED, and SRC, while Bicer and Dincer's configuration includes SOFC, IGCC, RC, and PEME subsystems. The proposed setup achieves an exergetic efficiency increase of 0.87 % and a thermal efficiency improvement of 4.08 % due to enhanced waste heat recovery through MED and SRC integration, which confirms its performative superiority.

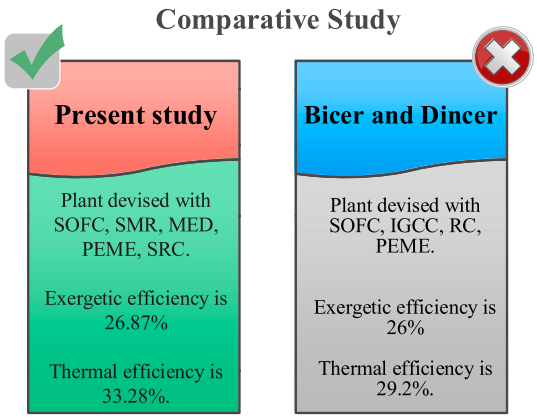

Fig. 13. The comparative reports of the presented assessment.

5. Conclusion

The current study introduced an innovative configuration aimed at generating power, freshwater, and hydrogen. The design comprised an SOFC fueled by methane steam reforming, a steam Rankine cycle, a MED unit, and a PEME. Operational metrics were evaluated through comprehensive thermodynamic, economic, and environmental examinations, complemented by parametric analysis and multi-objective optimization. The key findings of the study are summarized as follows.

- The SOFC and AB were reported as the primary causes of energy destruction, with respective rates of 474 kW and 498 kW. The rate of total exergy destruction was estimated at approximately 3662.32 kW.
- The AB and HX1 exhibited the highest cost rates associated with exergy destruction, while the steam turbine and SOFC had the highest total cost rates, amounting to 239,591.65 $/year and 109,050.25 $/year, respectively.
- The environmental assessments revealed a value of 14.48 Pt/h for the products' exergoenvironmental impact rate.
- The SOFC, steam turbine, and PEME accounted for the highest purchase costs, representing shares of 38.09 %, 17.33 %, and 13.32 %, respectively, of the total capital investment cost.
- The fuel utilization factor had a significant impact on net power generation and SUCP, while freshwater production rate and exergy efficiency were notably sensitive to the temperature of the stack flow.
- Although the $\eta_{ex} - \dot{m}_{fw}$ scenario provided a higher product rate, the SUCP $- \dot{m}_{fw}$ scenario demonstrated superior economic performance due to its lower capital investment cost and higher profit from product sales.
- The optimal state selected from the SUCP $- \dot{m}_{fw}$ scenario resulted in a net power generation of 1201.58 kW, a freshwater production rate of 0.95 kg/s, and a 0.0016 kg/s hydrogen production rate, which achieved a 29.86 % exergy efficiency, a 3.63-year payback period, and a 13.92 Pt/h exergoenvironmental impact rate.

Looking ahead, future assessments will focus on extending the current evaluations to dynamic and real-time operational examinations, incorporating energy storage structures and hybridizing with renewable energy integration to elevate the configuration's flexibility and sustainability. Moreover, exploring alternative fuels, advanced control approaches, and uncertainty-based thermoeconomic investigations will further support the development of resilient and region-specific multi-generation frameworks.

CRediT authorship contribution statement

Jing Wang: Writing – review & editing, Writing – original draft, Methodology, Funding acquisition, Formal analysis. **Yonghao Zeng:** Writing – review & editing, Writing – original draft, Validation, Software, Resources, Investigation. **Ming Wang:** Writing – review & editing, Writing – original draft, Supervision, Project administration, Data curation, Conceptualization.

Declaration of competing interest

The authors declare that they have no known competing financial interests or personal relationships that could have appeared to influence the work reported in this paper.

Acknowledgment

2024 Liaoning Province Natural Science Foundation Joint Fund Project; Research on Energy Storage Mechanism of Ion-Doped $Li_4Ti_5O_{12}$/PEO Composites for Solid Electrolytes; 20240321.

Appendix A. Supplementary data

Supplementary data to this article can be found online at https://doi.org/10.1016/j.energy.2025.137917.

Data availability

Data will be made available on request.

References

[1] Shokri A, Shakibi H, Azizi S, Yari M, Mahmoudi SMS. Optimization of biomass-fueled multigeneration system using SOFC for electricity, hydrogen, and freshwater production. Int J Hydrogen Energy 2024;88:1293–320. https://doi.org/10.1016/j.ijhydene.2024.09.161.
[2] Noorzadeh S, Yari M, Mahmoudi SMS. Assessing the thermoeconomic performance of a solar-powered trigeneration system with an upgraded transcritical carbon dioxide unit. Process Saf Environ Prot 2024;191:1035–58. https://doi.org/10.1016/j.psep.2024.09.024.
[3] Perera F. Pollution from fossil-fuel combustion is the leading environmental threat to global pediatric health and equity: solutions exist. Int J Environ Res Public Health 2018;15:16. https://doi.org/10.3390/ijerph15010016.
[4] Shu G, Liu L, Tian H, Wei H, Yu G. Parametric and working fluid analysis of a dual-loop organic rankine cycle (DORC) used in engine waste heat recovery. Appl Energy 2014;113:1188–98. https://doi.org/10.1016/j.apenergy.2013.08.027.
[5] Shuit SH, Tan KT, Lee KT, Kamaruddin AH. Oil palm biomass as a sustainable energy source: a Malaysian case study. Energy 2009;34:1225–35. https://doi.org/10.1016/j.energy.2009.05.008.
[6] Wang X, Mi X, Lv X, Weng Y. Fast and stable operation approach of ship solid oxide fuel cell-gas turbine hybrid system under uncertain factors. Int J Hydrogen Energy 2022;47:21472–91. https://doi.org/10.1016/j.ijhydene.2022.04.284.
[7] Rajeyyagari SR, Nowduri S. Optimizing solid oxide fuel cell performance using advanced meta-heuristic algorithms. Advances in Engineering and Intelligence Systems 2024;3:106–26. https://doi.org/10.22034/aeis.2024.460563.1202.
[8] Asgari A, Faal MY, Yari M, Mohebbi M, Mahmoodi R, Noorzadeh S. Optimizing Co-generation performance of reactivity controlled compression ignition engines with solar steam reforming of methanol; a thermoeconomic, economic and exergoenvironmental analysis. Int J Hydrogen Energy 2024;94:145–65. https://doi.org/10.1016/j.ijhydene.2024.10.419.

[9] Sadeghi M, Jafari M, Hajimolana YS, Woudstra T, Aravind PV. Size and exergy assessment of solid oxide fuel cell-based H2-fed power generation system with alternative electrolytes: a comparative study. Energy Convers Manag 2021;228:113681. https://doi.org/10.1016/j.enconman.2020.113681.

[10] Cammarata A, Dìaz Lacharme MC, Colbertaldo P, Donazzi A, Campanari S. Numerical and experimental assessment of a novel SOFC-Based system for micro-power generation. J Power Sources 2022;551:232180. https://doi.org/10.1016/j.jpowsour.2022.232180.

[11] Jiang P, Mahmud Parvez A, Meng Y, Dong X, Xu M, Luo X, et al. Novel two-stage fluidized bed-plasma gasification integrated with SOFC and chemical looping combustion for the high efficiency power generation from MSW: a thermodynamic investigation. Energy Convers Manag 2021;236:114066. https://doi.org/10.1016/j.enconman.2021.114066.

[12] Li C, Wang Z, Liu H, Guo F, Li C, Xiu X, et al. Exergetic and exergoeconomic evaluation of an SOFC-Engine-ORC hybrid power generation system with methanol for ship application. Fuel 2024;357:129944. https://doi.org/10.1016/j.fuel.2023.129944.

[13] Teng S, Hamrang F, Talesh SSA. Economic performance assessment of a novel combined power generation cycle. Energy 2021:121092.

[14] Hai T, Dahan F, Dhahad HA, Almojil SF, Alizadeh A, sharma A, et al. Deep-learning optimization and environmental assessment of nanomaterial's boosted hydrogen and power generation system combined with SOFC. Int J Hydrogen Energy 2024;52:202–15. https://doi.org/10.1016/j.ijhydene.2022.11.332.

[15] Cheng C, Cherian J, Sial MS, Zaman U, Niroumandi H. Performance assessment of a novel biomass-based solid oxide fuel cell power generation cycle; economic analysis and optimization. Energy 2021;224:120134. https://doi.org/10.1016/j.energy.2021.120134.

[16] Wang Z, Ma Y, Cao M, Jiang Y, Ji Y, Han F. Energy, exergy, exergoeconomic, environmental (4E) evaluation and multi-objective optimization of a novel SOFC-ICE-SCO2-HRSG hybrid system for power and heat generation. Energy Convers Manag 2023;291:117332. https://doi.org/10.1016/j.enconman.2023.117332.

[17] Liu G, Qin Y, Ji D. Enhancing geothermal ORC power generation with SOFC: a comprehensive parametric study on thermodynamic performance. Appl Therm Eng 2023;233:121161. https://doi.org/10.1016/j.applthermaleng.2023.121161.

[18] Zhu P, Wu Z, Guo L, Yao J, Dai M, Ren J, et al. Achieving high-efficiency conversion and poly-generation of cooling, heating, and power based on biomass-fueled SOFC hybrid system: performance assessment and multi-objective optimization. Energy Convers Manag 2021;240:114245. https://doi.org/10.1016/j.enconman.2021.114245.

[19] Ran P, Zhou X, Wang Y, Fan Q, Xin D, Li Z. Thermodynamic and exergetic analysis of a novel multi-generation system based on SOFC, micro-gas turbine, s-CO2 and lithium bromide absorption refrigerator. Appl Therm Eng 2023;219:119585. https://doi.org/10.1016/j.applthermaleng.2022.119585.

[20] Tian L, Zhang Z, Salah B, Marefati M. Multi-variable assessment/optimization of a new two-source multigeneration system integrated with a solid oxide fuel cell. Process Saf Environ Prot 2023;179:754–73. https://doi.org/10.1016/j.psep.2023.08.003.

[21] Liu Y, Han J, You H. Exergoeconomic analysis and multi-objective optimization of a CCHP system based on SOFC/GT and transcritical CO2 power/refrigeration cycles. Appl Therm Eng 2023;230:120686. https://doi.org/10.1016/j.applthermaleng.2023.120686.

[22] Uzair Azhar M, Anwar M, Khan UM, Hassan M, Muhammed Ali SA, Waqas A, et al. Thermodynamic analysis of different modes of a multigeneration SOFC-CCHP system with freshwater production and LNG cold energy utilization. Energy Convers Manag 2023;297:117730. https://doi.org/10.1016/j.enconman.2023.117730.

[23] Liu C, Han J, Liang W, Ge Y, Zhu W, Yang J, et al. Performance analysis and multi-objective optimization of a novel poly-generation system integrating SOFC/GT with SCO2/HDH/ERC. Appl Therm Eng 2024;238:122075. https://doi.org/10.1016/j.applthermaleng.2023.122075.

[24] Soleymani E, Gargari SG, Ghaebi H. Thermodynamic and thermoeconomic analysis of a novel power and hydrogen cogeneration cycle based on solid SOFC. Renew Energy 2021;177:495–518. https://doi.org/10.1016/j.renene.2021.05.103.

[25] Tukenmez N, Yilmaz F, Ozturk M. Parametric analysis of a solar energy based multigeneration plant with SOFC for hydrogen generation. Int J Hydrogen Energy 2022;47:3266–83. https://doi.org/10.1016/j.ijhydene.2021.01.131.

[26] Dai J, Abdulwahab A, Wei H, Alanazi A, Alanazi M, I Alanazi T, et al. Multi-criteria sensitivity study and optimization of an electricity/cooling/hydrogen production scheme combined with SOFC-Based sequential heat recovery: sustainability and economic analyses. Process Saf Environ Prot 2023;174:169–87. https://doi.org/10.1016/j.psep.2023.03.083.

[27] Yilmaz F, Ozturk M. Design and modeling of an integrated combined plant with SOFC for hydrogen and ammonia generation. Int J Hydrogen Energy 2022;47:31911–26. https://doi.org/10.1016/j.ijhydene.2022.01.249.

[28] Adebayo V, Abid M, Adedeji M, Ratlamwala TAH. Energy, exergy and exergo-environmental impact assessment of a solid oxide fuel cell coupled with absorption chiller & cascaded closed loop ORC for multi-generation. Int J Hydrogen Energy 2022;47:3248–65. https://doi.org/10.1016/j.ijhydene.2021.02.222.

[29] Wang H, Su Z, Abed AM, Nag K, Deifalla A, Marefati M, et al. Multi-criteria evaluation and optimization of a new multigeneration cycle based on solid oxide fuel cell and biomass fuel integrated with a thermoelectric generator, gas turbine, and methanation cycle. Process Saf Environ Prot 2023;170:139–56. https://doi.org/10.1016/j.psep.2022.11.087.

[30] Cao Y, Zoghi M, Habibi H, Raise A. Waste heat recovery of a combined solid oxide fuel cell-gas turbine system for multi-generation purposes. Appl Therm Eng 2021;198:117463. https://doi.org/10.1016/j.applthermaleng.2021.117463.

[31] Huang Z, Xiao Y, You H, Chen D, Hu B, Li G, et al. Performance analysis and multi-objective optimization of a novel solid oxide fuel cell-based poly-generation and condensation dehumidification system. Energy Convers Manag 2024;319:118935. https://doi.org/10.1016/j.enconman.2024.118935.

[32] Zheng S, Wu Z, Zhou X. Economic and environmental analysis of a new sustainable multi-generation system for power, heating, cooling, freshwater, and hydrogen production. Energy 2025;328:136465. https://doi.org/10.1016/j.energy.2025.136465.

[33] Zhuang Y, Jin T, Song M, Du J, Gu S. A kinetic model-based SOFC combined cycle power generation system for waste heat recovery. Front Chem Sci Eng 2025;19:35. https://doi.org/10.1007/s11705-025-2536-3.

[34] Hadelu LM, Boyaghchi FA. Exergoeconomic and exergoenvironmental analyses and optimization of different ejector based two stage expander-organic flash cycles fuelled by solar energy. Energy Convers Manag 2020;216:112943. https://doi.org/10.1016/j.enconman.2020.112943.

[35] Parikhani T, Jannatkhah J, Shokri A, Ghaebi H. Thermodynamic analysis and optimization of a novel power generation system based on modified kalina and GT-MHR cycles. Energy Convers Manag 2019;196. https://doi.org/10.1016/j.enconman.2019.06.018.

[36] Azizi S, Shakibi H, Shokri A, Chitsaz A, Yari M. Multi-aspect analysis and RSM-based optimization of a novel dual-source electricity and cooling cogeneration system. Appl Energy 2023;332:120487. https://doi.org/10.1016/j.apenergy.2022.120487.

[37] Hamrang F, Shokri A, Mahmoudi SMS, Ehghaghi B. Performance analysis of a new electricity and freshwater production system based on an integrated gasification combined cycle and Multi- effect desalination. https://doi.org/10.3390/su12197996; 2020.

[38] Sadeghi M, Chitsaz A, Marivani P, Yari M, Mahmoudi SMS. Effects of thermophysical and thermochemical recuperation on the performance of combined gas turbine and organic rankine cycle power generation system: thermoeconomic comparison and multi-objective optimization. Energy 2020;210:118551. https://doi.org/10.1016/j.energy.2020.118551.

[39] Eisavi B, Chitsaz A, Hosseinpour J, Ranjbar F. Thermo-environmental and economic comparison of three different arrangements of solid oxide fuel cell-gas turbine (SOFC-GT) hybrid systems. Energy Convers Manag 2018;168:343–56. https://doi.org/10.1016/j.enconman.2018.04.088.

[40] Ahmadi P, Dincer I, Rosen MA. Thermodynamic modeling and multi-objective evolutionary-based optimization of a new multigeneration energy system. Energy Convers Manag 2013;76:282–300. https://doi.org/10.1016/j.enconman.2013.07.049.

[41] Cengel YA, Boles MA, Kanoglu M. Thermodynamics: an engineering approach, vol. 5. New York: McGraw-hill; 2011.

[42] Hai T, Mansir IB, Mulki H, Anqi AE, Deifalla A, Chen Y. Integration of wind turbine with biomass-fueled SOFC to provide hydrogen-rich fuel: economic and CO2 emission reduction assessment. Process Saf Environ Prot 2023;170:946–59. https://doi.org/10.1016/j.psep.2022.12.049.

[43] Ni M, Leung MKH, Leung DYC. Parametric study of solid oxide steam electrolyzer for hydrogen production. Int J Hydrogen Energy 2007;32:2305–13. https://doi.org/10.1016/j.ijhydene.2007.03.001.

[44] AlZahrani AA, Dincer I. Design and analysis of a solar tower based integrated system using high temperature electrolyzer for hydrogen production. Int J Hydrogen Energy 2016;41:8042–56. https://doi.org/10.1016/j.ijhydene.2015.12.103.

[45] Santarelli MG, Torchio MF. Experimental analysis of the effects of the operating variables on the performance of a single PEMFC. Energy Convers Manag 2007;48:40–51. https://doi.org/10.1016/j.enconman.2006.05.013.

[46] Gurau V, Barbir F, Liu H. An analytical solution of a half-cell model for PEM fuel cells. J Electrochem Soc 2000;147:2468–77. https://doi.org/10.1149/1.1393555.

[47] Askari IB, Ameri M. Thermodynamic analysis of multi effect desalination unit with thermal vapor compression feed by different motive steam pressures. Desalination Water Treat 2020;184. https://doi.org/10.5004/dwt.2020.25387.

[48] Bejan A, Tsatsaronis G, Moran MJ. Thermal design and optimization. John Wiley & Sons; 1995.

[49] Habibollahzade A, Rosen MA. Syngas-fueled solid oxide fuel cell functionality improvement through appropriate feedstock selection and multi-criteria optimization using Air/O2-enriched-air gasification agents. Appl Energy 2021;286:116497. https://doi.org/10.1016/j.apenergy.2021.116497.

[50] Jia Y, Wang Y, Shang L. Optimizing a hybrid solid oxide fuel cell-gas turbine and geothermal energy system for enhanced efficiency and economic performance in power and hydrogen production scenario. Int J Hydrogen Energy 2024;84:246–64. https://doi.org/10.1016/j.ijhydene.2024.08.196.

[51] Azizi S, Nedaei N, Yari M. Proposal and evaluation of a solar-based polygeneration system: development, exergoeconomic analysis, and multi-objective optimization. Int J Energy Res 2022;46:13627–56. https://doi.org/10.1002/er.8084.

[52] Mohammadi Hadelu L, Ahmadi Boyaghchi F. Exergoeconomic and exergoenvironmental analyses and optimization of different ejector based two stage expander-organic flash cycles fuelled by solar energy. Energy Convers Manag 2020;216:112943. https://doi.org/10.1016/j.enconman.2020.112943.

[53] Ding Y, Liu C, Zhang C, Xu X, Li Q, Mao L. Exergoenvironmental model of organic rankine cycle system including the manufacture and leakage of working fluid. Energy 2018;145:52–64. https://doi.org/10.1016/j.energy.2017.12.123.

[54] Cheng Z-D, He Y-L, Du B-C, Wang K, Liang Q. Geometric optimization on optical performance of parabolic trough solar collector systems using particle swarm optimization algorithm. Appl Energy 2015;148:282–93. https://doi.org/10.1016/j.apenergy.2015.03.079.

[55] Tao G, Armstrong T, Virkar A. Intermediate temperature solid oxide fuel cell (IT-SOFC) research and development activities at MSRI. Nineteenth annual ACERC&ICES conference. 2005. Provo, UT.
[56] Hamrang F, Shokri A, Mahmoudi SM, Ehghaghi B, Rosen MA. Performance analysis of a new electricity and freshwater production system based on an integrated gasification combined cycle and multi-effect desalination. Sustainability 2020;12:7996. https://doi.org/10.3390/su12197996.
[57] Ioroi T, Yasuda K, Siroma Z, Fujiwara N, Miyazaki Y. Thin film electrocatalyst layer for unitized regenerative polymer electrolyte fuel cells. J Power Sources 2002;112:583–7. https://doi.org/10.1016/S0378-7753(02)00466-4.
[58] Bicer Y, Dincer I. Energy and exergy analyses of an integrated underground coal gasification with SOFC fuel cell system for multigeneration including hydrogen production. Int J Hydrogen Energy 2015;40:13323–37. https://doi.org/10.1016/j.ijhydene.2015.08.023.